Journal for ImmunoTherapy of Cancer

Dual checkpoint blockade of CD47 and PD-L1 using an affinity-tuned bispecific antibody maximizes antitumor immunity

Shih-Hsun Chen ,[1] Pawel K Dominik,[2] Jessica Stanfield,[1] Sheng Ding,[2] Wenjing Yang,[3] Nadia Kurd,[1] Ryan Llewellyn,[1] Jonathan Heyen,[4] Carole Wang,[2] Zea Melton,[2] Thomas Van Blarcom,[2] Kevin C Lindquist,[2] Javier Chaparro-Riggers,[2] Shahram Salek-Ardakani [1]

To cite: Chen S-H, Dominik PK, Stanfield J, *et al*. Dual checkpoint blockade of CD47 and PD-L1 using an affinity-tuned bispecific antibody maximizes antitumor immunity. *Journal for ImmunoTherapy of Cancer* 2021;**9**:e003464. doi:10.1136/jitc-2021-003464

► Additional supplemental material is published online only. To view, please visit the journal online (http://dx.doi.org/10.1136/jitc-2021-003464).

Accepted 30 August 2021

[1]Cancer Immunology Discovery, Pfizer Inc, San Diego, California, USA
[2]BioMedicine Design, Pfizer Inc, San Diego, California, USA
[3]Computational Biology, Pfizer Inc, San Diego, California, USA
[4]Drug Safety R&D, Pfizer Inc, San Diego, California, USA

Correspondence to
Dr Shih-Hsun Chen; Shih-Hsun.Chen@pfizer.com

Dr Javier Chaparro-Riggers; javier.chaparro-riggers@pfizer.com

Dr Shahram Salek-Ardakani; ssalekardakani@gmail.com

ABSTRACT

Background T cell checkpoint immunotherapies have shown promising results in the clinic, but most patients remain non-responsive. CD47-signal regulatory protein alpha (SIRPα) myeloid checkpoint blockade has shown early clinical activity in hematologic malignancies. However, CD47 expression on peripheral blood limits αCD47 antibody selectivity and thus efficacy in solid tumors.

Methods To improve the antibody selectivity and therapeutic window, we developed a novel affinity-tuned bispecific antibody targeting CD47 and programmed death-ligand 1 (PD-L1) to antagonize both innate and adaptive immune checkpoint pathways. This PD-L1-targeted CD47 bispecific antibody was designed with potent affinity for PD-L1 and moderate affinity for CD47 to achieve preferential binding on tumor and myeloid cells expressing PD-L1 in the tumor microenvironment (TME).

Results The antibody design reduced binding on red blood cells and enhanced selectivity to the TME, improving the therapeutic window compared with αCD47 and its combination with αPD-L1 in syngeneic tumor models. Mechanistically, both myeloid and T cells were activated and contributed to antitumor activity of αCD47/PD-L1 bispecific antibody. Distinct from αCD47 and αPD-L1 monotherapies or combination therapies, single-cell RNA sequencing (scRNA-seq) and gene expression analysis revealed that the bispecific treatment resulted in unique innate activation, including pattern recognition receptor-mediated induction of type I interferon pathways and antigen presentation in dendritic cells and macrophage populations. Furthermore, treatment increased the $Tcf7^{+}$ stem-like progenitor CD8 T cell population in the TME and promoted its differentiation to an effector-like state. Consistent with mouse data, the compounds were well tolerated and demonstrated robust myeloid and T cell activation in non-human primates (NHPs). Notably, RNA-seq analysis in NHPs provided evidence that the innate activation was mainly contributed by CD47-SIRPα but not PD-L1-PD-1 blockade from the bispecific antibody.

Conclusion These findings provide novel mechanistic insights into how myeloid and T cells can be uniquely modulated by the dual innate and adaptive checkpoint antibody and demonstrate its potential in clinical development (NCT04881045) to improve patient outcomes over current PD-(L)1 and CD47-targeted therapies.

BACKGROUND

The PD-1 immune checkpoint is well established in its ability to attenuate T cell-mediated immune responses in patients whose tumors express its ligand, programmed death-ligand 1 (PD-L1). While therapeutic interventions blocking PD-1 or PD-L1 can release antitumor T-cell immunity, the immune response remains suppressed in many tumors.[1] In patients harboring these types of tumors, increased antitumor activity cannot be established from PD-1/PD-L1 inhibition alone.[2] CD47, a cell surface molecule in the immunoglobulin superfamily, is another established target overexpressed on various malignant cells and has been described colloquially as the regulator of a 'don't-eat-me' signal.[3 4] CD47 binds to several proteins, including signal regulatory protein alpha (SIRPα), signal regulatory protein gamma (SIRPγ), integrins, and thrombospondin-1.[5] When bound to its receptor, SIRPα, which is present on various myeloid cells, CD47 acts as an innate inhibitory checkpoint by interrupting the phagocytosis of tumor cells and downstream activation of innate responses.[4] By suppressing innate immune activation and presentation of tumor antigens and priming of T cell responses, CD47 may enable tumor cells to escape both innate and adaptive immune surveillance.[6] *MYC* oncogene, deregulated in >50% of human cancers, has been found to upregulate both CD47 and PD-L1 expression on the surface of tumor cells by binding to their promoters.[7] CD47 overexpression has also been shown to act as a resistance mechanism to PD-1/PD-L1 therapies in preclinical models.[8 9] Thus, CD47 has become an attractive target, with various approaches to block CD47/SIRPα interactions in clinical development.[10]

Treatment with monospecific αCD47 antibodies has been particularly successful in hematological malignancies, such as non-Hodgkin's lymphoma (NHL).[11] Patients with NHL of various cell types treated with αCD47 achieved an objective response rate of 50%–70%, with complete response rates of 36%–40% and markedly increased overall survival.[11] Unfortunately, limited efficacy has thus far been observed in patients with solid tumors[12] even when αCD47 was combined with αPD-1/PD-L1 agents.[9] One explanation for the lack of efficacy in solid tumors is the inability to effectively target the tumor, as CD47 is widely expressed on circulating erythroid, myeloid, and other cells of hemopoietic origin. The high therapeutic doses that would be required have shown the potential to cause significant anemia through increased phagocytosis of red blood cells (RBCs). If the binding of αCD47 to RBCs could be reduced, it might be possible to ameliorate anemia and provide a new method to reverse the innate immunosuppression of myeloid cells by tumors.

We generated an affinity-tuned bispecific antibody (BisAb) targeting CD47 and PD-L1 to antagonize both innate and adaptive immune checkpoint pathways. This novel BisAb was designed with potent affinity for PD-L1 and reduced affinity for CD47 to achieve preferential binding on tumor and myeloid cells expressing PD-L1 in the tumor microenvironment (TME), thus increasing tumor exposure for potent antitumor efficacy and reducing the risk of anemia. The BisAb using an IgG with full effector function further enhanced tumor-killing activity *in vitro* and *in vivo*. Moreover, the unique binding selectivity of αCD47/PD-L1 resulted in a distinct macrophage and dendritic cell (DC) activation and an increase in stem-like progenitor and effector $CD8^+$ T cells in the TME, compared with the combination treatment of monospecific αCD47 and αPD-L1 antibodies. Thus, this study provides insight into how myeloid cells and T cells can be uniquely modulated by the dual innate and adaptive checkpoint antibody and demonstrate its potential in clinical development (NCT04881045).

MATERIALS AND METHODS

In vivo mouse models

CT26 cells in serum-free phosphate-buffered saline (PBS) were inoculated in the right flank at 2.5×10^5 cells per implant and allowed to grow for 14 days. MC38 or B16F10 cells in serum-free PBS were inoculated in the right flank at 5×10^5 cells per implant and allowed to grow for 7–10 days (MC38) or 9–13 days (B16F10). The mice were then randomized by tumor volume and treated with the described antibodies. Length and width of tumors were recorded using digital caliper measurements. Tumor volume was calculated using the formula tumor volume = $\text{width}^2 \times 0.5(\text{Length})$. Percent of initial body weight was calculated using the formula % of initial body weight=bodyweight day post-treatment initiation (g)/body weight D0 post-treatment initiation (g) × 100. Percent survival post-treatment was determined using the Kaplan-Meier survival curve in GraphPad Prism. Mice were euthanized if tumor size exceeded 2000 mm^3 or had a body weight loss greater than 20% of initial body weight.

Unless otherwise stated, the following treatment antibodies were used for syngeneic tumor experiments: mouse IgG2a isotype control antibody from BioXcell (C1.18.4), and Pfizer in-house generated anti-mouse CD47 antibody (αmCD47), anti-mouse PD-L1 antibody (αmPD-L1), mouse BisAb (mBisAb) or mBisAb mIgG2a Fc null. All antibodies were diluted in PBS and administered intraperitoneally (i.p.). For CT26 antitumor efficacy, survival and bodyweight loss studies, female Balb/c tumor bearing mice were randomized at day 14 post-inoculation. For single agent treatment groups, treatment antibodies were administered at 5 mg/kg. For the combination treatment group, 5 mg/kg of αmCD47 and 5 mg/kg of αmPD-L1 were administered. Treatment antibodies were administered every 3–4 days for a total for three doses (days 0, 3 and 7 post-treatment initiation). For B16F10 antitumor efficacy, female C57/Bl6 tumor bearing mice were randomized at day 9 post inoculation. Treatment antibodies were administered at 20 mg/kg three times a week for a total for nine doses (3Qw ×3 weeks). For MC38 dose-dependent antitumor efficacy in C57/BL6 tumor-bearing mice were randomized at day 7 post-inoculation. Treatment antibodies were administered every 3–4 days for a total of six doses (days 7, 9, 12, 15, 22 and 26 post-tumor inoculation). mBisAb was administered at 10 mg/kg, 20 mg/kg, and 40 mg/kg. Tumors were measured as above twice a week. For MC38 antitumor efficacy with immune cell depletion, female C57/BL6 tumor bearing mice were randomized at day 6 post-inoculation. Vehicle control (PBS) and mBisAb mIgG2a was administered at 40 mg/kg every 3–4 days for a total of six doses (Days 7, 11, 14, 18, 21, 25 post-tumor inoculation). Depletion antibodies were diluted in PBS and administered i.p at 200 ug/mouse on day 6 post-tumor inoculation and every 2–3 days thereafter until the termination of the study for a total of nine doses. The following depletion antibodies were from BioXcell: anti-CD8 (clone 2.43) antibody, anti-CD4 (GK1.5) antibody, anti-NK1.1 (clone PK136) antibody or anti-CSF1R (clone AFS93) antibody. For MC38 antitumor efficacy in $Batf3^{-/-}$ mice, female $Batf3^{-/-}$ tumor bearing mice were randomized at day 10 post-inoculation. Mouse IgG2a isotype control and mBisAb mIgG2a were administered at 10 mg/kg every 3–4 days for a total of four doses (days 10, 13, 17, 20 post-tumor inoculation).

For in vivo binding selectivity, male human FcγR B16F10 tumor bearing mice were randomized at day 13 post-inoculation. Treatment antibodies were generated in-house at Pfizer. The following treatment antibodies were diluted in PBS and administered at 10 mg/kg at days 13 and 16 post-inoculation for a total of two doses: human IgG isotype control, αmCD47 hIgG1, αmPD-L1 hIgG1 and mBisAb hIgG1. Blood and tumor tissue were collected on day 18 post inoculation to assess treatment antibody binding selectivity assessment by flow cytometry.

To assess impact of murine RBCs on treatment, treatment antibodies were administered to male Balb/c mice at 5 mg/kg twice (days 0 and 3). The peripheral blood was collected 2 days post second dose (day 5) and red blood counts were assessed.

Non-human primate models

Cynomolgus monkeys were administrated either vehicle or test-article by slow bolus intravenous injection on study day 1 and day 8. Animals were monitored twice daily for clinical observations and body weights collected on a weekly basis. Scheduled collections of peripheral blood for clinical pathology evaluation included hematology and clinical chemistry assessments. For gene expression analysis, peripheral blood was collected in RNAprotect tubes (Qiagen) according to manufacturer's instructions for RNA sequencing (RNA-seq).

Statistical analyses

Statistical analysis was applied to biologically independent mice or technical replicates for each experiment. For antitumor efficacy studies, the statistical significance of tumor volumes between experimental groups was calculated using a two-way analysis of variance (ANOVA) with multiple comparison using GraphPad Prism V.8 software. The ordinary one-way ANOVA or Student's unpaired T cells were used for statistical calculations using GraphPad Prism V.8 software for other statistical analysis as specified in figure legends. All error bars were reported as mean±SEM. The level of significance is indicated as *p<0.05; **p<0.01; ***p<0.001.

More detailed information is available in online supplemental material section.

RESULTS

Design and characterization of αCD47/PD-L1 BisAb

αCD47/PD-L1 is a fully human BisAb (hBisAb) in an IgG_1 format using knobs-in-holes technology and a common light chain architecture (figure 1A). Each binding arm was discovered independently using synthetic common light chain phage display libraries[13] in two campaigns against extracellular domains of human CD47 and human PD-L1 (figure 1B). After several rounds of optimization, affinity tuning, and liability removal of each binding arm, the final human αCD47/PD-L1 hBisAb with moderate affinity to CD47 and highly potent affinity to PD-L1 was reformatted and purified using standard biochemical procedures. To confirm the dual binding activity of hBisAb to each antigen, the kinetic rate constants were measured by surface plasmon resonance (SPR). The K_D of hBisAb to human and cynomolgus monkey CD47 was 59.5 nM and 83.9 nM, respectively, and the K_D to human and monkey PD-L1 was 0.227 nM and 0.231 nM, respectively (online supplemental table 1). The EC_{50} of binding to each target was determined using cell-based binding assays. The binding of the hBisAb to human CD47 ectopically expressed on CHO cells was reduced (CD47 EC_{50}=11.89 nM) (figure 1C) compared with the binding of the hBisAb to human PD-L1 expressed on CHO cells (PD-L1 EC_{50}=0.32 nM) (figure 1D). The increased potency of the PD-L1 EC_{50} compared with the CD47 EC_{50} of the hBisAb is aligned with the design of the antibody in which the goal was to develop a BisAb with a moderate affinity to CD47 and highly potent affinity to PD-L1. Despite a reduced affinity for human CD47, hBisAb potently inhibited the interaction of human SIRPα/CD47 as determined by SPR (online supplemental table 1) and in cell-based assays, where hBisAb blocked the binding of SIRPα to CHO-hCD47 cells (figure 1E) with an IC_{50} of 123.6 nM. Additionally, hBisAb efficiently blocked the interaction of human PD-1/PD-L1 as determined by SPR (online supplemental table 1). The ability of hBisAb to enhance T cell functionality by blocking the PD-1/PD-L1 interaction was also measured by a PD1-PD-L1 T-cell receptor (TCR) nuclear factor of activated T cell (NFAT) reporter assay. The average EC_{50} induced by hBisAb was 0.451 nM with no statistical difference compared with other human αPD-L1 bivalent antibodies (αhPD-L1) (figure 1F).

We next performed coculture assays of human $CD47^+PD\text{-}L1^+$ tumor cells and monocyte-derived macrophages to examine the impact of hBisAb on antibody-dependent cellular phagocytosis (ADCP). We found that hBisAb induced a greater increase in phagocytosis of tumor cells than αhCD47 or αhPD-L1 monotherapy (online supplemental figure 1A), suggesting that engaging both targets on tumor cells increased the efficiency of phagocytic activity. We also compared the activity of hBisAb in the context of IgG_1 and IgG_4, two IgG isotypes related to phagocytosis. We found that the hBisAb-mediated enhancement of ADCP was significantly more potent with IgG_1 than IgG_4 (figure 1G). Furthermore, to determine the role of SIRPα/CD47 and PD-1/PD-L1 in DC-mediated T cell activation, we performed a mixed lymphocyte reaction (MLR). In the MLR assay, αhCD47 treatment reduced interleukin 2 (IL-2) secretion while αhPD-L1 single agent treatment and its combination with αhCD47 increased IL-2 secretion (figure 1H). Interestingly, treatment with hBisAb showed a significant increase in IL-2 (figure 1H) and interferon γ (IFNγ) secretion (online supplemental figure 1B) compared with single and combination treatments, demonstrating the superior capacity of hBisAb to enhance DC-mediated T cell activation.

The αCD47/PD-L1 BisAb preferentially binds cells expressing PD-L1 in the TME, reducing binding to PD-L1 negative circulating RBCs

To determine the binding selectivity of the BisAb in vitro, $CD47^+PD\text{-}L1^+$ human cancer cell line HT-1080 was cocultured with human RBCs, which only express CD47 (figure 2A). The hBisAb demonstrated >1500 fold reduced binding to RBCs (EC_{50}=7.37 nM) compared with tumor cells (EC_{50}=0.0047 nM). In contrast, monospecific αhCD47 antibodies showed similar binding to both tumor and RBCs, with average tumor cell binding EC_{50} values

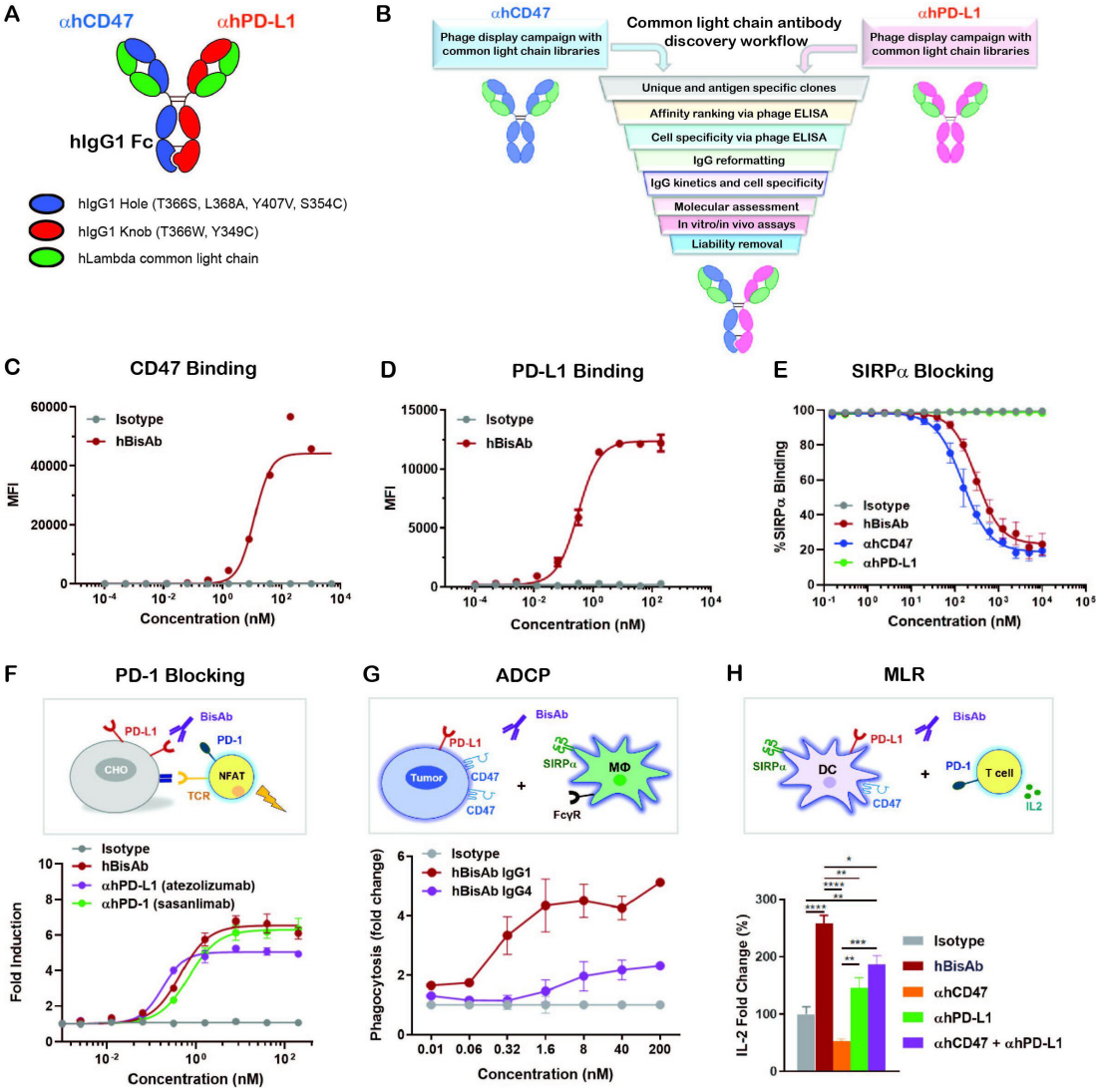

Figure 1 Design and characterization of αCD47/PD-L1 bispecific antibody. (A) The schematic diagram of the human αCD47/PD-L1 bispecific antibody (hBisAb). (B) Workflow of common light chain antibody campaign for the generation of hBisAb. (C, D) Cell based binding of hBisAb on CHO-hCD47 (C), and CHO-hPD-L1 (D), as measured by flow cytometry. (E) In vitro blocking activity of hBisAb on the human CD47/SIRPα interaction as measured by flow cytometry. (F) In vitro blocking activity of hBisAb on the human PD-L1/PD-1 interaction using a PD-L1/PD-1 TCR blocking reporter bioassay. The blocking activity was quantified and normalized as the fold change compared with isotype control. (G) Phagocytosis of NCI-H292 human tumor cells by human monocyte-derived macrophages in the presence of human IgG isotype control, hBisAb in IgG_1 or IgG_4 format (n=2 donors/group). Phagocytosis of total tumor cells is represented as fold change compared with isotype treatment. (H) MLR assay was conducted to assess concentration of IL-2 at 72 hours in the supernatant by ELISA. A mixture of LPS matured DCs and purified $CD4^+$ T cells were cocultured at a 1:4 ratio in the presence of αhCD47, αhPD-L1, the combination of αhCD47 and αhPD-L1, or hBisAb at 200 nM. *P<0.05, **p<0.01, ***p<0.001, ****p<0.0001, one-way ANOVA. ADCP, antibody-dependent cellular phagocytosis; ANOVA, analysis of variance; DC, dendritic cell; IL-2, interleukin 2; MLR, mixed lymphocyte reaction; LPS, lipopolysaccharide; TCR, T cell receptor.

from 0.006 nM to 0.031 nM and RBC binding EC_{50} values from 0.027 nM to 1.17 nM (figure 2B). Due to a lack of cross-reactivity of the hBisAb to mouse CD47 or PD-L1, we generated mouse surrogates of αCD47/PD-L1 (mBisAb) with comparable in vitro binding selectivity to tumor cells versus RBCs and blocking activities of CD47/SIRPα and PD-L1/PD-1 as hBisAb (figure 2D and E, online supplemental figure 1C,D). We then used the mBisAb to examine the binding selectivity of BisAb in vivo. αmCD47, αmPD-L1, or mBisAb were administrated in mice inoculated with B16F10 tumor cells expressing CD47 and PD-L1.[14] The peripheral blood and tumor were harvested to investigate the antibody distribution among RBCs, tumor cells and tumor-infiltrating leucocytes (TILs). As expected, most RBCs were bound by anti-mouse CD47 bivalent antibodies (αmCD47) with minimal binding on tumor cells or TILs (figure 2E). αmPD-L1 bivalent antibodies tend to bind both murine tumor and immune cells in TME with no binding on RBCs. The mBisAb binding on RBCs was

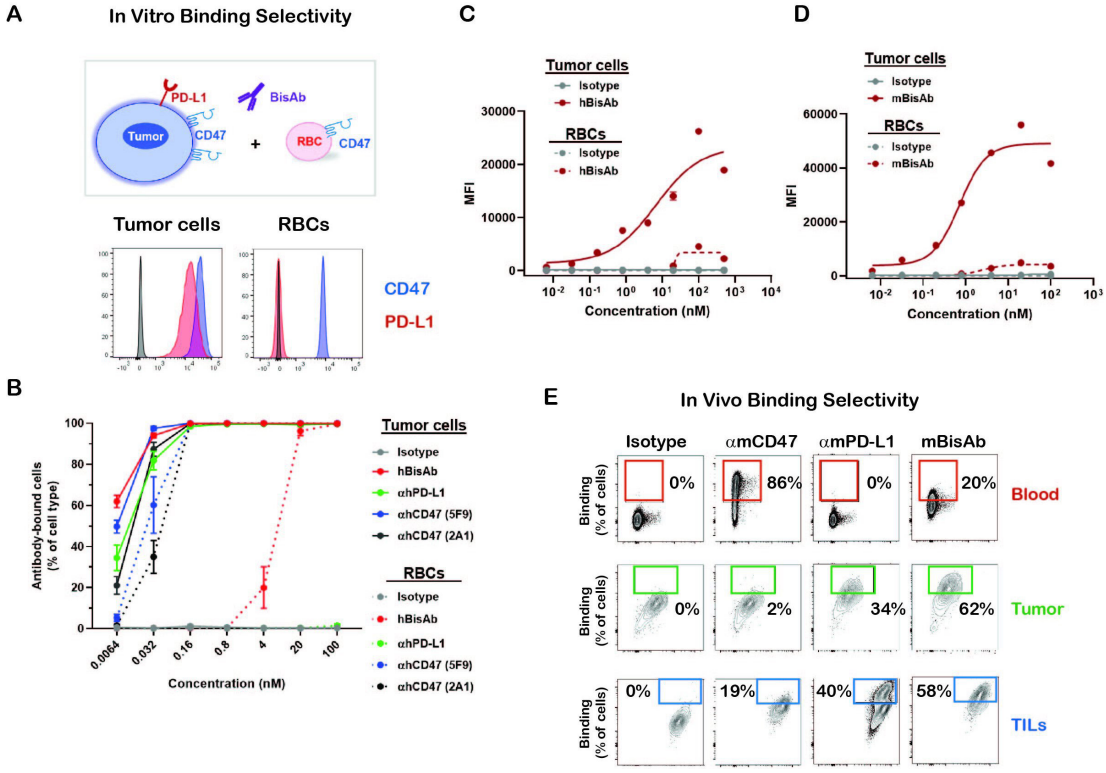

Figure 2 The binding selectivity of αCD47/PD-L1 bispecific antibody (A, B) The binding selectivity of hBisAb on tumor cells and RBCs in vitro. The human tumor cell line HT-1080 and RBCs were stained for CD47 and PD-L1 expression by flow cytometry (A). CSFE-labeled HT-1080 tumor cells were cocultured with RBCs in the presence of indicated antibodies and binding selectivity was measured as the percentage of antibody-bound cells per cell type by flow cytometry (B). All experiments were repeated at least twice. (C) Cell-based binding of hBisAb on human tumor cell line HT-1080 and human RBCs in vitro as measured by flow cytometry. (D) Cell-based binding of mBisAb on murine tumor cell line MC38 and murine RBCs in vitro as measured by flow cytometry. (E) The binding selectivity of the αCD47/PD-L1 mouse surrogate mBisAb *in vivo*. Human FcγR mice bearing subcutaneous B16F10 tumors were dosed IP on days 13 and 16 post-tumor inoculation with αmCD47, αmPD-L1, or mBisAb in human IgG isotype. Blood and tumor tissues were collected at day 18 and therapeutic antibody binding was assessed using an anti-human IgG secondary antibody by flow cytometry (n=3 mice/group).CFSE, carboxyfluorescein succinimidyl ester; hBisAb, human bispecific antibody; IP, intraperitoneally; RBC, red blood cell; TILs, tumor-infiltrating leucocytes.

markedly reduced compared with αmCD47 (figure 2E; top panel). In contrast, binding on both tumor cells and TILs was significantly increased relative to αmCD47 (figure 2E; middle and bottom panel), indicating that the PD-L1 arm of the BisAb mediates enhanced selectivity for cells in the TME. Notably, mBisAb exhibited enhanced binding to tumor cells compared with αmPD-L1, demonstrating that the bispecific approach improved targeting of tumor cells over either monotherapy.

αCD47/PD-L1 BisAb inhibits tumor growth with better therapeutic window compared with the combination of αCD47 and αPD-L1 and is mediated by CD8+ T cells and DCs in syngeneic models

The antitumor activity of targeting CD47 and PD-L1 in a bispecific format was evaluated in various syngeneic murine tumor models. In the CT26 tumor model with the same antibody doses between groups, mBisAb showed superior tumor growth inhibition than either αmCD47 or αmPD-L1 antibody alone (figure 3A). In addition, an Fc-null version of mBisAb (with inactive mouse IgG2a) exhibited reduced tumor growth inhibition compared with mBisAb with wild-type Fc, suggesting that IgG effector function plays a role in the mBisAb-mediated therapeutic effect (figure 3A). Furthermore, with the same antibody doses between groups the survival rate (75%) of the mBisAb-treated cohort was significantly improved compared with the cohorts treated with αmCD47 (12.5%), αmPD-L1 (12.5%) or their combination (62.5%) (figure 3B), demonstrating that the bispecific approach may provide a more favorable survival benefit. Notably, the administration of mBisAb was tolerated in mice throughout the study with no impact on body weight (figure 3C). Meanwhile, with the same antibody dose, αmCD47 single agent or its combination with αmPD-L1 resulted in transient but significant body weight loss. To further elucidate the potential impact on hematology mediated by CD47-targeting therapeutics, as has been previously described in preclinical models and the clinic,[3 12] the blood from each cohort was harvested

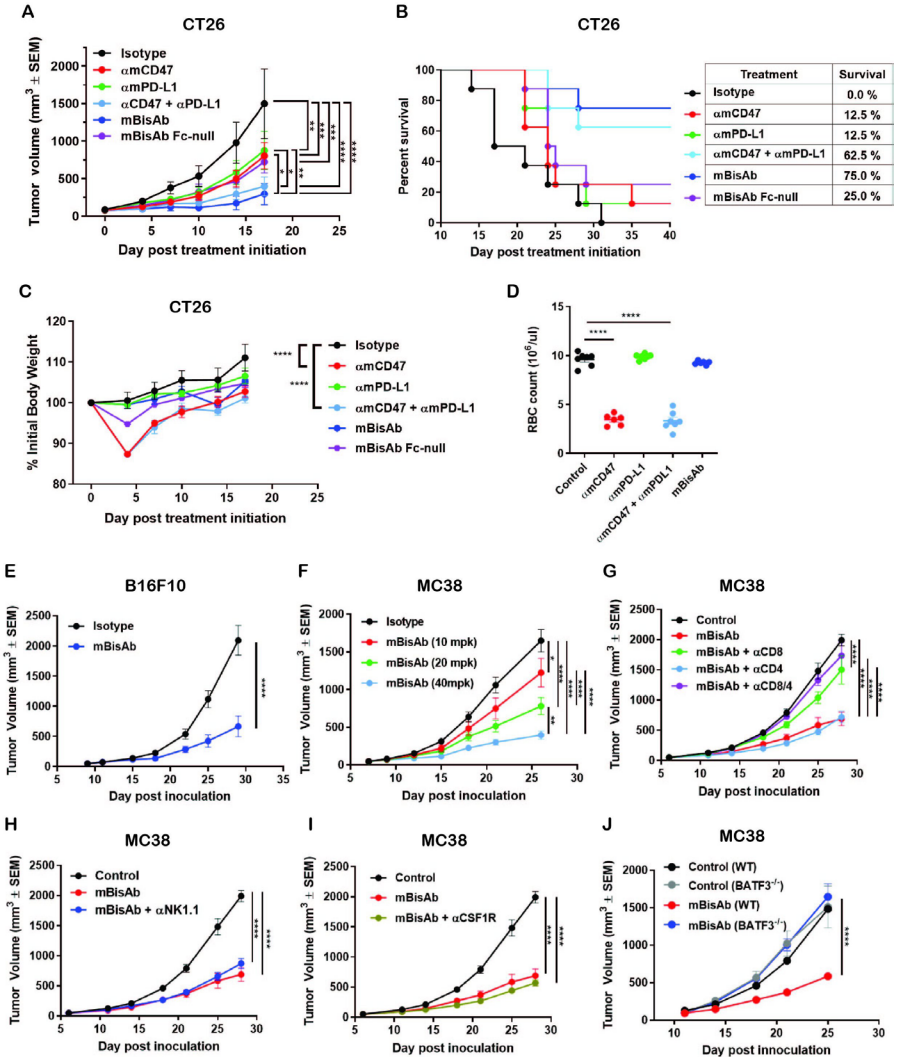

Figure 3 The therapeutic effect of αCD47/PD-L1 mouse surrogates in syngeneic tumor models. (A–C) Antitumor efficacy, survival and body weight post treatment of indicated antibodies in CT26 tumor model. BALB/c mice bearing subcutaneous CT26 tumors were dosed IP with 5 mg/kg of mIgG2a isotype, 5 mg/kg of αmCD47, 5 mg/kg of αmPD-L1, the combination of 5 mg/kg of αmCD47 and 5 mg/kg of αmPD-L1, or 5 mg/kg of mBisAb on days 0, 3, and 7 post-treatment initiation (n=7–8 mice/group). (A) Tumor growth; significance was calculated by two-way ANOVA with Tukey's multiple comparison test. (B) Kaplan-Meier survival curves post-treatment initiation. (C) Percent of initial body weight reported as a mean±SEM; significance was calculated by two-way ANOVA with Tukey's multiple comparison test compared with isotype control. (D) BALB/c mice were dosed IP on day 0 and 3 with the same concentration in (A–C). Red blood cells from whole blood on day 5 were counted (n=6–7 mice/group). Significance was calculated by ordinary one-way ANOVA compared with control. (E) Antitumor efficacy in B16F10 tumor model. C57BL/6 mice bearing subcutaneous B16F10 tumors were treated on 9 days post-inoculation with isotype control or mBisAb three times a week for 3 weeks (n=10 mice/group). Significance was calculated by two-way ANOVA with Sidak's multiple comparison test. (F) Dose-dependent antitumor efficacy in MC38 tumor model. C57BL/6 mice bearing subcutaneous MC38 tumors were treated 7 days postinoculation and dosed IP every 3–4 days for 3 weeks with 10, 20, and 40 mg/kg of mBisAb (n=10 mice/group). Significance was calculated by two-way ANOVA with Tukey's multiple comparison test. (G–I) Antitumor efficacy following mBisAb treatment and immune cell depletion in MC38 model. MC38-bearing mice were dosed with vehicle (control) or mBisAb every 3–4 days for a total of six doses. Depletion antibodies were administrated IP 1 day prior to treatment with mBisAb and dosed three times a week throughout the study. (n=8–10 mice/group). Significance was calculated by two-way ANOVA with Tukey's multiple comparison test. (J) C57BL/6 wildtype (WT) and Batf3$^{-/-}$ mice bearing subcutaneous MC38 tumor were dosed IP every 3–4 days for 3 weeks with mBisAb (n=8 mice/group). Significance was calculated by two-way ANOVA with sidak's multiple comparison test. Asterisks indicate statistical significance (*p<0.05, **p<0.01, ***p<0.001, ****p<0.0001). ANOVA, analysis of variance; αmPD-L1, anti-mouse PD-L1 antibody; αmCD47, anti-mouse CD47 antibody; mBisAb, αCD47/PD-L1 mouse surrogate; IP, intraperitoneally.

after the second dose when the transient body weight loss appeared. The number of mouse RBCs was significantly reduced in the cohorts treated with αmCD47 alone and in combination with αmPD-L1 (figure 3D). At the same time, there was no significant difference in the

mBisAb-treated group compared with isotype control, indicating that the bispecific targeting approach enhances antitumor efficacy and reduces potential toxicity effects. Single-agent antitumor activity was also demonstrated in B16F10, an immunologically cold tumor model resistant to anti-PD-(L)1 treatment (figure 3E).[8 15] Furthermore, the mBisAb resulted in a robust dose-dependent efficacy in the MC38 tumor model (figure 3F).

To further investigate the mechanism underlying mBisAb-mediated antitumor activity, a series of antibody-based immune cell depletion studies were performed in MC38 tumor-bearing mice. We found that depletion of $CD8^+$, but not $CD4^+$ T cells, abrogated antitumor efficacy of mBisAb (figure 3G). In contrast, depletion of either natural killer (NK) cells or macrophages alone did not impact antitumor efficacy (figure 3H,I). Interestingly, the mBisAb-mediated tumor growth inhibition was also abolished in $Batf3^{-/-}$ mice (figure 3J). Given that BATF3 has been shown to intrinsically regulate the generation of CD8 T cell memory in the context of infection,[16] we cannot rule out the influence of BATF3 deficiency on T cells in this model. However, since targeting the CD47 axis depends on a well-established role for DCs in mediating antitumor efficacy,[17 18] it is likely that the therapeutic effect of the bispecific involves both $CD8^+$ T cells and DCs.

αCD47/PD-L1 BisAb treatment induces a robust systemic $CD8^+$ T cell response and expansion of the intratumoral $CD8^+$ T cell pool

We next investigated the impact of mBisAb treatment on individual immune subsets by performing CyTOF analysis. MC38-bearing mice were treated with isotype (control) or mBisAb every 3–4 days starting at day 10 post-tumor implantation, and tumors and spleens were harvested at day 15, 20, or 25. Intratumoral leucocyte populations were first identified using common lineage-defining markers (online supplemental figure 2A-D),[19] and the relative representation of these populations was determined over time (online supplemental figure 2E). We noted an increase in the frequency of CD8 T cells among total $CD45^+$ cells in the tumors of mBisAb-treated mice (online supplemental figure 2E). Within the myeloid compartment, only modest changes in expression of markers typically associated with activation state were observed after mBisAb treatment, except for the apparent transient loss of CX3CR1 and Fc receptor expression (online supplemental figure 2F, compare day 15, 20, and 25). We also observed the same trend for PD-L1 staining in mBisAb-treated tumors and spleens at these time points, which may reflect competition for epitope binding in the presence of mBisAb.

To further understand which T cell compartments are influenced following mBisAb treatment (figure 3G), we generated viSNEs exclusively on T cells (live $CD45^+$C-$D19^-NK1.1^-CD3^+$) from either the spleens (figure 4A–D) or tumors (figure 4E–H) of mBisAb and control-treated mice at day 20 post-tumor implantation, the peak of mBisAb-mediated intratumoral T cell expansion (figure 4G). Compared with control-treated mice, there was a clear enrichment in $CD8^+$ T cells with an activated phenotype ($CD44^{hi}$, $CD62L^{lo}$, $CX3CR1^+$, $KLRG1^+$, T-bet^+, $Eomes^+$) in the spleens of mBisAb-treated mice (figure 4A,B). We noted a proportional increase in $CD8^+$ T cells expressing KLRG1 and CX3CR1, markers associated with effector T cell responses, among total $CD8^+$ T cells in the spleen of mBisAb-treated mice beginning at day 20 post-implantation, which remained elevated at day 25 (figure 4C,D). We also noted an increase in a population of activated conventional $CD4^+$ T cells ($FoxP3^-CD44^{hi}CD62L^{lo}$) expressing high levels of CX3CR1 (figure 4A,B, online supplemental figure 3A). We further validated these findings using flow cytometry, and found a significant increase in the numbers of activated proliferating ($CD44^+Ki67^+$) $CD8^+$ T cells in the spleen on mBisAb treatment, which was not observed on αmCD47 or αmPD-L1 treatment (online supplemental figure 3B). Notably, the frequency of $CD103^+$ cells within cDC1 was also increased in the spleen of mBisAb-treated mice (online supplemental figure 3C). We also found elevated levels of several pro-inflammatory mediators in the serum of mBisAb-treated mice, including IL-1β, IL-12, and IL-18, key cytokines that support $CD8^+$ T cell priming and activation, as well as the key T cell effector cytokine IFNγ (online supplemental table 2). These data suggest that mBisAb promotes increased accumulation of migratory cDC1s in the spleen and a robust systemic T cell response, increasing proinflammatory and effector cytokines systemically. Furthermore, the importance of these increases in migratory cDC1 and effector CD8 T cells induced by mBisAb treatment is highlighted by the loss of antitumor efficacy in the absence of CD8 T cells or Batf3-dependent DCs during mBisAb treatment (figure 3G,J).

Among intratumoral T cells, the viSNE analysis revealed a shift toward a higher proportion of $CD8^+$ T cells and a relatively lower proportion of Tregs on mBisAb treatment (figure 4E,F). We further validated these findings by flow cytometry and found that absolute numbers of $CD8^+$ T cells within the tumor were significantly increased by mBisAb treatment compared with control, as well as αmCD47 or αmPD-L1 treatment (online supplemental figure 3D). Although there was a consistent decrease in the proportion of Tregs among T cells in mBisAb-treated tumors, the absolute number of Tregs remained unchanged between mBisAb, αmCD47, αmPD-L1, and control-treated tumors (figure 4H, online supplemental figure 3E). However, this resulted in a significant increase in the $CD8^+$ T cell/Treg ratio in mBisAb-treated but not αmCD47 or αmPD-L1-treated tumors, a measure that has been associated with an effective antitumor response and favorable prognosis (online supplemental figure 3E).[20 21] To gain a greater mechanistic understanding of how mBisAb bolstered the intratumoral $CD8^+$ T cell response, we performed comparative gene expression analysis on MC38 tumor tissues of control or mBisAb-treated mice on day 20 post-tumor implantation by Nanostring. We found that mBisAb-treated tumors had a higher representation of gene expression signatures related to $CD8^+$ T cell effector function and

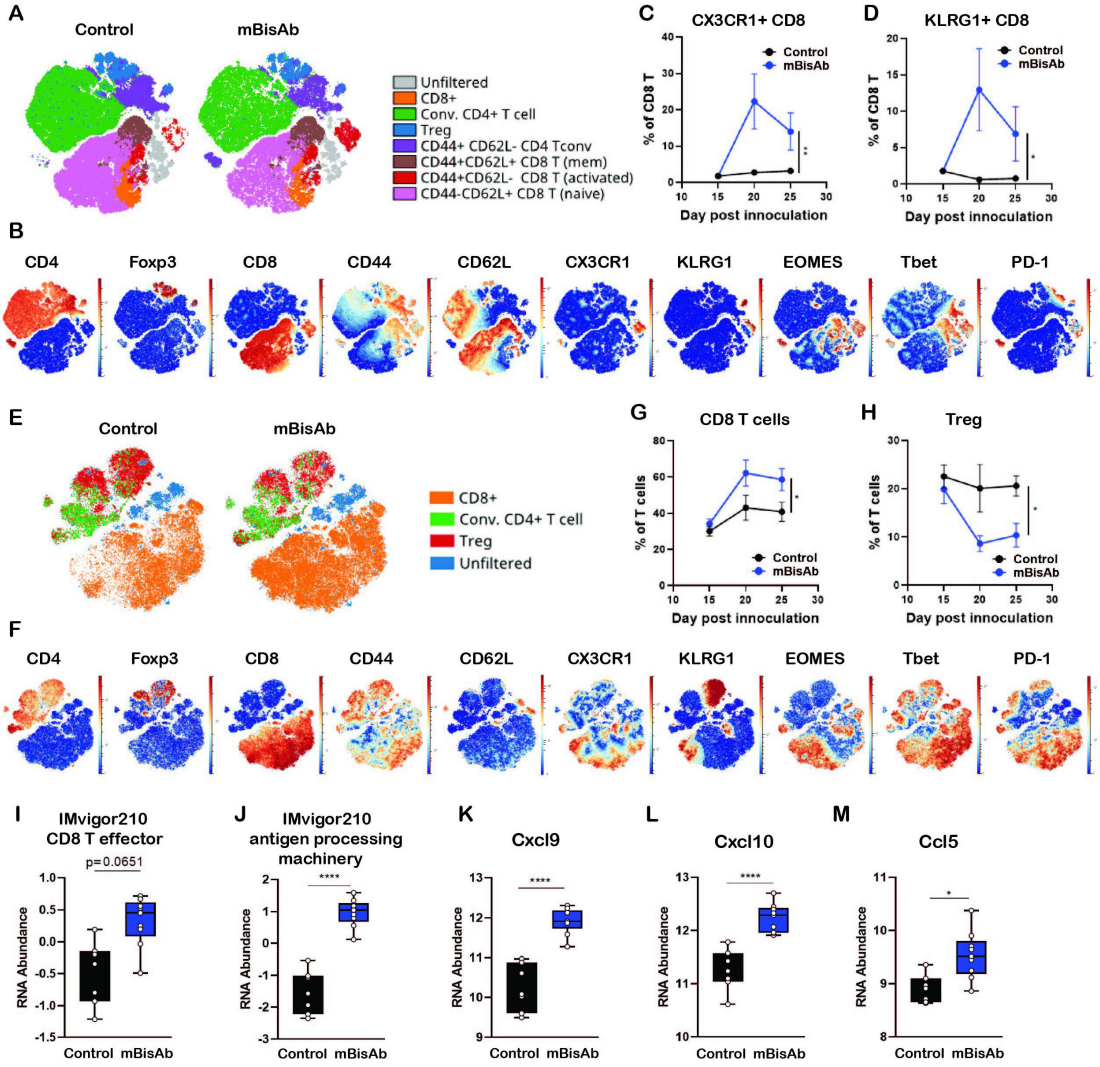

Figure 4 Immunopharmacodynamics of αCD47/PD-L1 mouse surrogate treatment by CyTOF and Nanostring (A–F) MC38-bearing mice were treated with isotype (control) or mBisAb every 3–4 days starting at day 10 post-tumor implantation, and tumors and spleens were harvested at day 15, 20, or 25 and prepared for analysis by CyTOF (n=5 mice/group). (A) ViSNE analysis of total T cells from the spleen of control (left) or mBisAb (right)-treated mice at day 20 post-tumor implantation. Indicated subsets were defined by biaxial gating and position of cells in each subset on the viSNE is represented by a unique color. (B) Expression of indicated markers among total splenic T cells, with each cell in the viSNE colored according to its MMI (mean marker intensity) value of the indicated marker. (C, D) Frequency of CX3CR1$^+$ (C) or KLRG1$^+$ (D) cells among total CD8$^+$ T cells in the spleens of control (black) or mBisAb-treated (blue) mice at the indicated time points. *P<0.05, **p<0.01, Mixed-effects analysis. (E) ViSNE analysis of total T cells from tumors of control or mBisAb-treated mice at day 20 post-tumor implantation. Indicated subsets were defined by biaxial gating and position of cells in each subset on the viSNE is represented by a unique color. (F) Expression of indicated markers among total intratumoral T cells, with each cell in the viSNE colored according to its MMI value of the indicated marker (G, H) Frequency of CD8$^+$ T cells (G) or Tregs (H) among total T cells in control (black) or mBisAb-treated (blue) tumors at the indicated timepoints. *P<0.05, **p<0.01, Mixed-effects analysis. (I–M) MC38-bearing mice were treated with control or mBisAb every 3–4 days starting at day 10 post-tumor implantation. Tumors were harvested at day 20 and prepared for gene expression analysis by Nanostring. Relative RNA abundance of effector CD8$^+$ T cell signature (I) and antigen processing machinery in IMvigor 210 dataset (J). Relative RNA abundance of *cxcl9* (K), *cxcl10* (L), and *ccl5* (M). *P<0.05, ****p<0.0001, Ordinary one-way ANOVA with tukey's multiple comparison test. ANOVA, analysis of variance; CyTOF, cytometry by time of flight.

antigen processing machinery (figure 4I,J).[22] The levels of crucial T cell-recruiting chemokines *Cxcl9*, *Cxcl10*, and *Ccl5*, were also elevated (figure 4K–M, online supplemental table 3) in mBisAb-treated tumors. These data suggest that the mBisAb could augment intratumoral CD8$^+$ T cell responses by enhancing the recruitment of CD8$^+$ T cells into the tumor and enhancing the presentation of tumor antigens.

αCD47/PD-L1 BisAb treatment reprograms myeloid populations and drives innate activation in the TME

In addition to the enrichment of gene signatures related to T cell activity, we identified many enriched genes in pathways related to innate immune activation in mBisAb-treated tumors. These include type I IFN signaling, pattern recognition receptor (PRR)-mediated induction of IFNα

pathways, and FcγR-dependent phagocytosis (figure 5A,B, online supplemental table 3). Using pathway correlation network analysis, we found that several pathways related to innate immune sensing, including toll-like receptor-mediated signaling, were specifically enriched among genes upregulated following mBisAb treatment compared with the combination treatment of αmCD47 and αmPD-L1 (online supplemental figure 4A). Thus, the bispecific targeting approach has distinct impacts on the TME that cannot be recapitulated by blocking CD47 and PD-L1 via separate antibodies.

To further elucidate the cellular source of the transcriptional changes in the TME, we next performed single-cell RNA-seq (scRNA-seq) analysis of MC38 tumors following treatment with mBisAb, αmCD47 alone, αmPD-L1 alone, or the combination of αmPD-L1 and αmCD47. The cell-type identity of each cluster was defined by the expression of lineage markers (online supplemental figure 4B,C).[19] While most treatment conditions minimally impacted the relative distribution of these populations, we noted an increased frequency of T cells following mBisAb treatment (online supplemental figure 4D). Unsupervised clustering identified six monocyte and macrophage populations (figure 5C), for which differential gene expression analysis revealed characteristic gene signatures that distinguished these clusters (figure 5D, online supplemental figure 5A, table 4). Cluster 5 cells comprised non-classical and classical monocyte populations, while the other clusters likely represent monocyte-derived cells, supported by trajectory analysis (figure 5E). Cluster 1 cells exhibited coexpression of immature monocyte genes *Ly6c2* and *Ccr2* and the maturation markers *Itgax* and *Cx3cr1*.[23] Cluster 2 and 4 were identified as tumor-associated macrophage (TAM) populations, characterized by markers for mature macrophages (*Vcam1, Mertk, Apoe*) and proliferation (*Top2a, Mki67*). Cluster 3 was distinctly enriched for angiogenic and inflammatory markers (*Vegfa, Nos2, Mmp12*). Cluster 6 cells exhibited expression of markers typically associated with immunosuppression (*Mrc1, Cd200r1*). While there were no significant changes in the relative frequency of myeloid clusters following treatment, distinct gene expression changes within these clusters were observed (figure 5F, online supplemental figure 5B–D). Notably, following mBisAb treatment, TAM populations exhibited an increase in the relative expression of genes associated with antigen processing and presentation, concomitant with a decrease in gene expression typically associated with cell cycle and proliferation (figure 5F, online supplemental figure 5B–D, table 4). Gene ontology (GO) pathway analysis comparing mBisAb versus control-treated tumors further illustrated upregulation of genes associated with antigen presentation, response to IFN, and complement activation in multiple myeloid populations (figure 5G, online supplemental figure 5E–J, table 4).

Unbiased clustering also revealed three subsets of conventional DCs (figure 5H) with gene expression profiles corresponding to cDC1, cDC2, and the recently described mregDC[24] populations (figure 5I, online supplemental table 4). Interestingly, mBisAb treatment-induced gene expression changes were similar to those induced by combination treatment of αmCD47 and αmPD-L1 in cDC1 (figure 5J). In contrast, an increase in the relative expression of genes associated with DC differentiation, response to type II IFN, and antigen processing and presentation was observed only in mBisAb-treated cDC2 subsets (figure 5K, online supplemental figure 5K, table 4). Of note, unlike cDC1 cells, cDC2 subsets reportedly coexpress PD-L1 and SIRPα,[25] the cognate ligand for CD47, suggesting that this population may be directly impacted by mBisAb therapy. We also noted that compared with other treatments, mBisAb administration induced gene expression changes related mainly to the regulation of translation within the mregDC subset (online supplemental figure 5K).

αCD47/PD-L1 BisAb treatment increases the frequency of stem-like progenitor and effector CD8$^+$ T cell subsets in the tumor and promotes the differentiation of progenitor CD8$^+$ T cells to an effector-like state

Consistent with our flow cytometry data, we observed significant increases in intratumoral CD8$^+$ T cell populations upon mBisAb treatment by scRNA-seq (online supplemental figure 4D). We next leveraged our scRNA-seq dataset to further understand how mBisAb treatment impacted CD8$^+$ T cells within the TME. We identified six distinct clusters of intratumoral CD8$^+$ T cells (figure 6A). To better understand how these clusters were distinguished from one another, we determined genes that were differentially expressed by each cluster relative to all other intratumoral CD8 T cell clusters (figure 6A,B, online supplemental figure 5). Several genes more highly expressed by CD8$^+$ T cell cluster 1, including the transcription factor *Tcf7* and the chemokine receptor *Cxcr3*, are characteristic of the recently characterized stem-like progenitor CD8$^+$ T cell population. This population has been shown to play a critical role in sustaining an effective antitumor T cell response and is correlated with improved responsiveness to checkpoint blockade therapy.[26–28] CD8$^+$ T cell cluster 1 cells also had a lower expression of genes typically associated with T cell exhaustion, including the transcription factor *Tox* and the inhibitory receptors *Pdcd1* (encoding PD-1), *Lag3*, and *Havcr2* (encoding Tim-3), while CD8$^+$ T cell clusters 2 and 3 had relatively high expression of exhaustion-associated genes (figure 6B, online supplemental figure 6A). Notably, CD8$^+$ T cell cluster 3 also had higher expression of genes associated with CD8$^+$ T cell effector functions, including *Ifng* and *Prf1* (encoding perforin), as well as the chemokines *Ccl4* and *Ccl3*, which have been shown to play a role in promoting DC and macrophage recruitment, maturation, and activation.[29 30] In addition, CD8$^+$ T cell cluster 3 also had a higher expression of *Cx3cr1* (figure 6B, online supplemental figure 6A). This marker has been shown to mark a subset of T cells in chronic viral

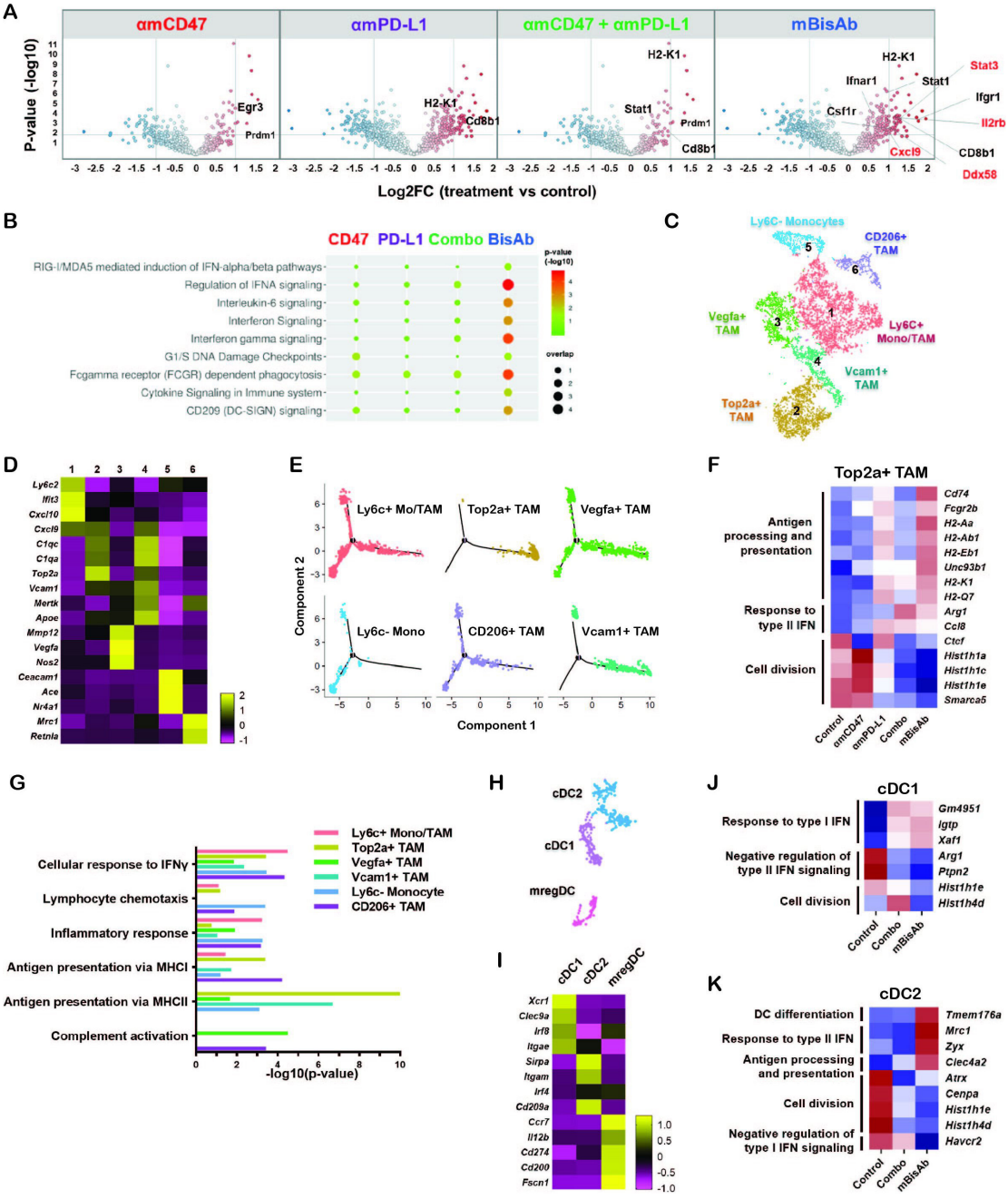

Figure 5 αCD47/PD-L1 mouse surrogate treatment reprograms myeloid populations and drives innate activation in tumor microenvironment (A, B) MC38-bearing mice were treated with the indicated antibodies every 3–4 days starting at day 10 post-tumor implantation. Tumors were harvested at day 20 and prepared for gene expression analysis by Nanostring. Volcano plots show log2 fold change of gene expression in the indicated treatment groups with DEGs compared with the control group (A). REACTOME pathway analysis in the indicated treatment groups compared with the control group (B). (C–K) MC38 tumor-bearing mice were treated with the same condition in (A) and tumor tissues were harvested for gene expression analysis using scRNA-seq. (C) tSNE analysis of intratumoral CD45$^+$ cells from all treatment conditions indicating six distinct clusters of monocyte/macrophage cells. (D) Heatmap displaying the average expressions of the selected DEGs for each cluster of monocyte/macrophage cells relative to other clusters. (E) Single-cell trajectory analysis by Monocle2 of the indicated populations. (F) Relative expression across treatment groups for selected genes that are differentially expressed among Cluster 2 Top2a$^+$ TAM in mBisAb-treated vs control-treated tumors. (G) Bar graph showing selected hits from GO pathway analysis performed on genes upregulated in myeloid clusters from mBisAb-treated tumors relative to the controls. (H) tSNE analysis of intratumoral CD45$^+$ cells from across all treatment conditions, cropped on 3 clusters of DCs. (I) Heatmap displaying the expression of the selected DEGs for each cluster of DC relative to other clusters. (J–K) Relative expression across treatment groups for selected genes that are differentially expressed in mBisAb-treated vs control-treated tumor DC clusters. DC, dendritic cell; DEG, differentially expressed gene; GO, gene ontology; IFN, interferon; MHC, major histocompatibility complex; scRNA-seq, single-cell RNA sequencing; TAM, tumor-associated macrophage; tSNE, t-distributed stochastic neighbor embedding.

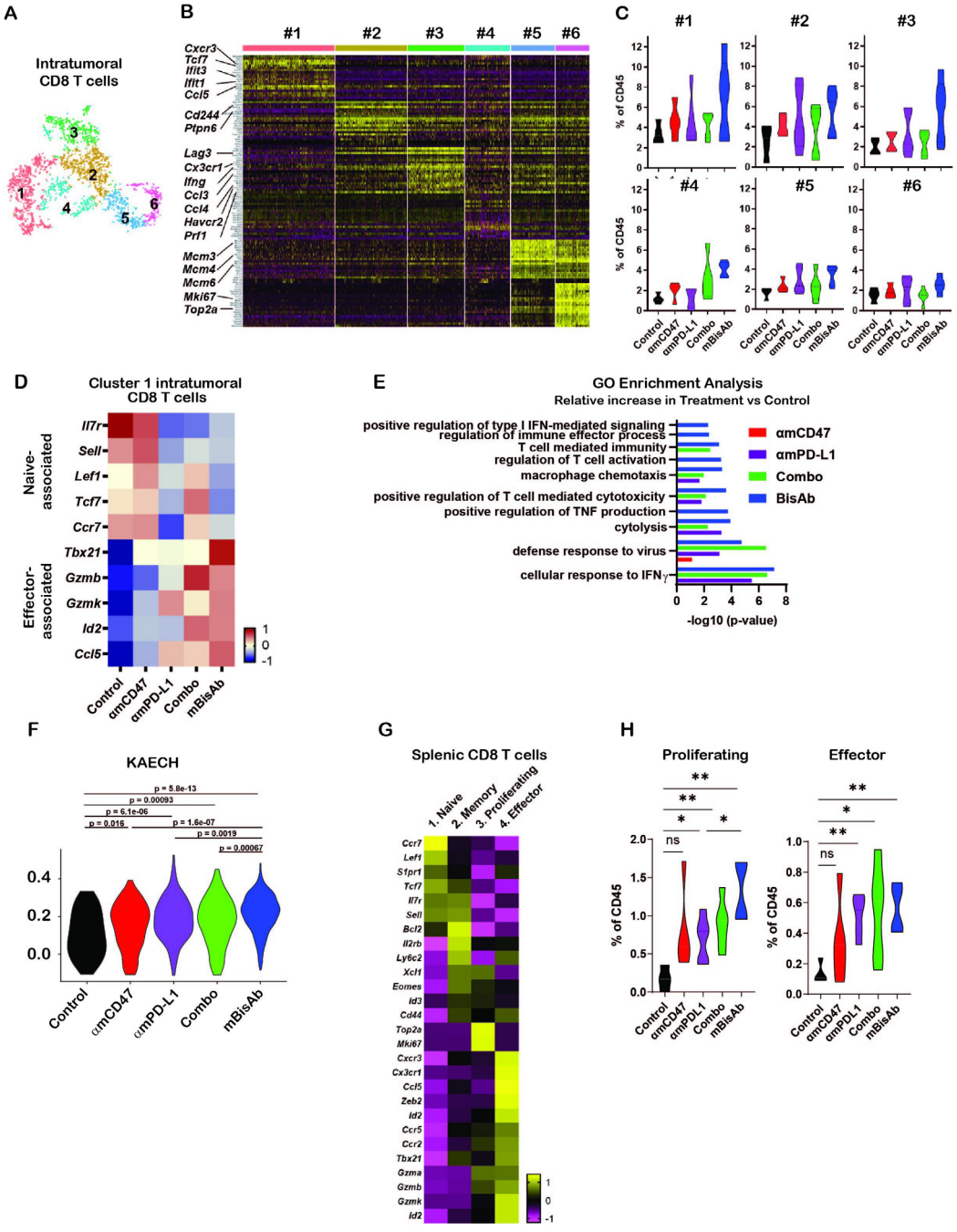

Figure 6 Impact of αCD47/PD-L1 mouse surrogate treatment on intratumoral and splenic T cell compartments (A–K) scRNA-seq samples in figure 5C–K were analysed for CD8$^+$ T cells. (A) tSNE analysis of intratumoral CD45$^+$ cells from across all treatment conditions, cropped on CD8$^+$ T cells, showing six distinct clusters of intratumoral CD8$^+$ T cells. (B) Heatmap displaying the expression of the top 20 DEGs for each cluster of intratumoral CD8$^+$ T cells relative to all other CD8$^+$ T cell clusters. Each column represents an individual cell in the indicated cluster, and each row represents an individual gene. (C) Frequency of each intratumoral CD8$^+$ T cell cluster among total CD45$^+$ cells in each treatment condition. (D) Relative average expression of selected genes that are differentially expressed among cluster 1 CD8$^+$ T cells in mBisAb-treated versus control-treated tumors, shown across all treatment conditions. (E) Selected hits from TopGO pathway analysis performed on genes differentially expressed by cluster 1 CD8$^+$ T cells from mBisAb-treated tumors relative to controls, with -log(10)p value for each pathway among genes differentially expressed by αmCD47, αmPD-L1, or combination-treated tumors relative to controls shown for comparison. No bar indicates that pathway was not significant for the given gene set. (F) Violin plots depicting the relative representation of the KAECH_NAIVE_VS_DAY8_EFF_CD8_TCELL_DN geneset in cluster 1 intratumoral CD8$^+$ T cells across treatment conditions. (G) Heatmap displaying the average expression of selected genes that are differentially expressed among each splenic CD8$^+$ T cell clusters relative to all other CD8$^+$ T cell clusters. (H) Frequency of proliferating and effector splenic CD8$^+$ T cell clusters among total CD45$^+$ cells in spleens from control, αmCD47, αmPD-L1, combination, and mBisAb-treated mice. *P<0.05; **P<0.01, Student's unpaired t-test. GO, gene ontology; IFN, interferon; ns, not significant; TNF, tumor necrosis factor.

infection with high effector functions distinct from terminally exhausted cells.[31 32] It has also been correlated with a positive response to checkpoint blockade therapy.[33 34]

In contrast, CD8+ T cell cluster 2 had a relatively higher expression of *Cd244*, a cell surface marker expressed highly on terminally exhausted cells,[32] and *Ptpn6* (encoding SHP-1) (figure 6B, online supplemental figure 6A). This protein phosphatase inhibits TCR signaling and is a crucial mediator of inhibitory signaling downstream of checkpoint receptors, including PD-1 and B- and T-lymphocyte attenuator.[35] Together, these gene expression patterns suggest that while cluster 2 cells may be terminally exhausted, cluster 3 cells retain the potential for high effector function. Notably, mBisAb treatment specifically increased the frequency of cluster 1 stem-like progenitor and cluster 3 effector-like CD8+ T cells to a greater extent than αCD47 and αPD-L1 monotherapies or combination therapies (figure 6C).

We validated the mBisAb-induced increase in the intratumoral stem-like progenitor CD8+ T cell population using flow cytometry (online supplemental figure 6B,C). We found a robust increase in both the frequency of the stem-like progenitor ($Tcf1^{hi}Lag3^{lo}$) population among antigen-experienced ($CD44^{hi}CD62L^{lo}$) intratumoral CD8+ T cells (online supplemental figure 6B) and in the total numbers of stem-like progenitor CD8+ T cells within the tumors of mBisAb-treated animals (online supplemental figure 6C). To further investigate the impact of mBisAb treatment on this population, we identified genes differentially expressed by cluster 1 CD8+ T cells in the tumors of control versus mBisAb-treated, αmCD47-treated, αmPD-L1-treated, or αmCD47 and αmPD-L1 combination-treated mice. Specific genes downregulated by CD8+ T cell cluster 1 following mBisAb treatment included genes associated with a naïve T cell state, such as the transcription factors *Tcf7*, *Lef1*, and *Bach2* (figure 6D). In contrast, genes upregulated by CD8+ T cell cluster 1 following mBisAb treatment included genes associated with effector CD8 T cell function and fate such as granzymes (*Gzmb*, *Gzmk*), immune cell-recruiting chemokines (*Ccl5*), and transcription factors *Tbx21* and *Id2* (figure 6D, online supplemental table 6).

We next performed GO enrichment analysis on these gene sets (online supplemental table 6) and found that following αmPD-L1, αmPD-L1 and αmCD47-combination, and mBisAb, but not αmCD47, treatment, genes more highly expressed by intratumoral CD8+ T cell cluster 1 were enriched in several pathways related to T cell differentiation and effector function, including cellular response to IFNγ, cytolysis, and T cell-mediated cytotoxicity (figure 6E, online supplemental table 6). However, many of these pathways were more significantly enriched following mBisAb treatment compared with other treatment conditions, and mBisAb treatment also resulted in an enrichment of additional pathways, such as regulation of T cell activation, positive regulation of TNF production, and positive regulation of type I IFN-mediated signaling, which were not enriched in other treatment conditions (figure 6E, online supplemental table 6). We also performed gene set enrichment analysis on genes differentially expressed by cluster 1 CD8+ T cells in the tumors of control vs mBisAb-treated mice. We found enrichment in many pathways associated with differentiation of CD8+ T cells from a naïve to effector state (online supplemental figure 6D, table 6). For example, the gene set most highly represented among genes upregulated by cluster 1 cells following mBisAb treatment was more highly expressed by CD8+ T cells at the peak of acute viral infection than the naïve state (online supplemental figure 6B).[36] We compared the collective representation of this gene set within cluster 1 CD8+ T cells across treatment conditions, and we observed the highest representation among cluster 1 CD8+ T cells following mBisAb treatment (figure 6F). Taken together, these findings suggest that mBisAb treatment not only expands the intratumoral stem-like progenitor CD8+ T cell population but also expands a population with high effector potential, perhaps by enhancing the differentiation of the stem-like progenitor population to an effector-like state. Moreover, treatment with mBisAb induced these effects more robustly than αmCD47 or αmPD-L1 monotherapy, as well as their combination.

We also leveraged our scRNA-seq dataset to investigate how mBisAb treatment impacted the splenic CD8+ T cell population. We identified four distinct clusters of CD8+ T cells within the spleen (online supplemental figure 6E). To elucidate the identity of each cluster, we determined the genes that were differentially expressed by each cluster relative to all other splenic CD8+ T cell clusters (figure 6G, online supplemental figure 6E, table 7). Splenic cluster 1 CD8+ T cells exhibited relatively higher expression of genes associated with naïve T cells, including *Lef1*, *Tcf7*, *Sell*, and *Il7r*. In contrast, cluster 2 expressed intermediate levels of these genes in addition to relatively higher expression of genes associated with a memory-like fate, including *Cd44*, *Ly6c2*, *Eomes*, and *Il2rb*. Splenic cluster 3 CD8+ T cells exhibited high expression of genes associated with cell cycle, such as *Mki67* and *Top2a*, suggesting that cells in this cluster were actively proliferating. Splenic cluster 4 CD8+ T cells exhibited high expression of genes associated with effector CD8+ T cell function and fate, including key lineage-defining transcription factors (*Tbx21*, *Zeb2*, and *Id2*), effector molecules (*Gzma*, *Gzmb*, *Gzmk*), and chemokine receptors (*Ccr5*, *Cxcr3*, *Cx3cr1*) (figure 6G, online supplemental table 7). We, therefore, defined splenic CD8+ T cell clusters 1, 2, 3, and 4 as naïve, memory, proliferating, and effector, respectively.

We next investigated how mBisAb treatment impacted the frequencies of these distinct CD8+ T cell populations by comparing the frequency of each cluster among total CD45+ cells in control,αmCD47, αmPD-L1, αmPD-L1 and αmCD47-combination, and mBisAb -treated spleens. We observed that αmPD-L1, αmPD-L1 and αmCD47-combination, and mBisAb, but not αmCD47-treatment, resulted in an increase in the frequency of both

proliferating and effector CD8+ T cell clusters relative to control-treated spleens (figure 6H). Notably, mBisAb treatment, but not αmPD-L1 and αmCD47-combination treatment, resulted in a significantly higher increase in proliferating splenic CD8 T cells than PD-L1 treatment (figure 6H). Consistent with our CyTOF and flow cytometry data (figure 4A–D, online supplemental figure 3B), these data reveal that mBisAb treatment induces both a robust systemic, as well as intratumoral, T cell response.

The administration of the αCD47/PD-L1 BisAb modulates both innate and adaptive immunity in cynomolgus monkeys

A non-human primate (NHP) study was conducted to explore the toxicity profile and potential pharmacodynamic markers of the hBisAb. The hBisAb demonstrated comparable binding and activity to cynomolgus monkey CD47 and PD-L1 (online supplemental table 1), making it suitable for *in vivo* experimentation. NHPs were administrated weekly intravenous doses of vehicle, 10, 30, or 100 mg/kg of hBisAb for 2 weeks. All dose levels were well tolerated during the in-life portion, with no notable clinical signs or changes in food consumption. Time course evaluation of circulating cell populations (standard hematology) following administration of hBisAb revealed minimal non-dose-dependent reductions of circulating RBCs and hemoglobin, and transient modulations of platelets. Absolute cell counts remained in the range of historical controls during the 2-week dosing period, and no changes were considered adverse (figure 7A,B, online supplemental figure 7A). Flow cytometry endpoints supported pharmacological modulation of critical immune effector cells. NHPs following administration of the hBisAb showed significant increases in $CD25^+CD8^+$ T cells (figure 7C) and $CD69^+CD4^+$ T cells (figure 7D), indicating that hBisAb modulates immune cell populations including T cell activation.

To further elucidate the immune modulation induced by hBisAb, we also performed gene expression analysis in NHP peripheral blood samples by bulk RNA-seq. Samples were collected at multiple time points, including pre-first/post-first dose (day 1) and pre-second/post-second dose (day 8) of hBisAb and vehicles over 2 weeks (figure 7E). Using principal component analysis (PCA) of the bulk RNA-seq data, the hBisAb and vehicle-treated samples clustered separately (online supplemental figure 7B). Analysis of the top differentially expressed genes (DEGs) between hBisAb and vehicle-treated samples revealed that hBisAb treatment increased the expression of genes associated with type I IFN signaling (*STAT1, BATF2, IRF7, RSAD2, IFIT3*) and myeloid cell activation (*CD80, MX1, TMEM173, DDX58*) (figure 7E, online supplemental figure 7D, table 8). Furthermore, many genes related to T cell activation (*CD28, ICOS, LAG3, CTLA4*) and cell migration (*CXCL10, CCR7*) were also enriched in the hBisAb cohort (figure 7E, online supplemental figure 7C,D). Indeed, ingenuity pathway analysis (IPA) of the top DEGs identified IFN signaling and PRR-mediated innate immune responses as the most enriched pathways in hBisAb cohorts relative to vehicle controls (figure 7F, online supplemental figure 7E). Using gene correlation network analysis among top upregulated DEGs in hBisAb-treated samples, *STAT1 and STAT2* were identified with the most connections as a hub (online supplemental figure 7F). These findings are consistent with preclinical and clinical reports showing that upregulation of *STAT1* on immune cells in the tumor is positively correlated with response to αPD-(L)1 therapy in melanoma and urothelial cancer.[22 37 38]

To deconvolute which hematopoietic cell types are responsible for the immune-modulating effects of hBisAb treatment, we applied the LM22 gene signature, a specific gene signature that can distinguish between 22 immune cell subsets, to our datasets. Interestingly, among all immune subsets, activated DCs and M1 macrophage phenotypes are the most enriched gene signature in hBisAb-treated samples relative to vehicle (figure 7G,H). These data are consistent with the TME data in mouse models (figure 5) and clinical evidence in patients[39] that innate immune modulation, particularly the type I IFN response, renders tumors sensitive to current immune checkpoint inhibitors.

To further elucidate the relative contributions of the CD47 and PD-L1 arms of hBisAb to the enrichment of innate activation pathways observed on treatment, we performed gene expression analysis in samples treated with a version of hBisAb, which has reduced CD47 affinity (hBisAb2) in part of the NHP studies. IPA analysis comparing the two hBisAb with different CD47 affinities revealed a distinct enrichment in pathways related to type I IFN signaling and myeloid cell activation among samples treated with hBisAb relative to hBisAb2 (figure 7I). Consistent with this, hBisAb induced the upregulation of several key innate immune-modulating genes which were not induced by hBisAb2 (figure 7J). Taken together, these findings indicate that the CD47 arm is the primary driver of the robust innate immune activation induced by hBisAb treatment.

DISCUSSION

Mounting evidence has shown that antagonizing the CD47-SIRPα myeloid checkpoint can prevent tumor cell evasion from innate immune surveillance. However, the liability of targeting CD47/SIRPα using a monospecific antibody approach is the hematological antigen sink and toxicity.[11] The ubiquitous expression of CD47 on normal cells, especially RBCs, significantly reduces the exposure of therapeutic antibodies on solid tumors overexpressing CD47. In this study, we described a novel affinity-tuned αCD47/PD-L1 BisAb with three key features. First, the design of moderate CD47 and potent PD-L1 affinity for the bispecific improved its selectivity to the TME versus peripheral blood. Second, the bispecific treatment resulted in a more favorable therapeutic window than αCD47, αPD-L1 monotherapy, or their combination in syngeneic tumor models. The administration of αCD47/

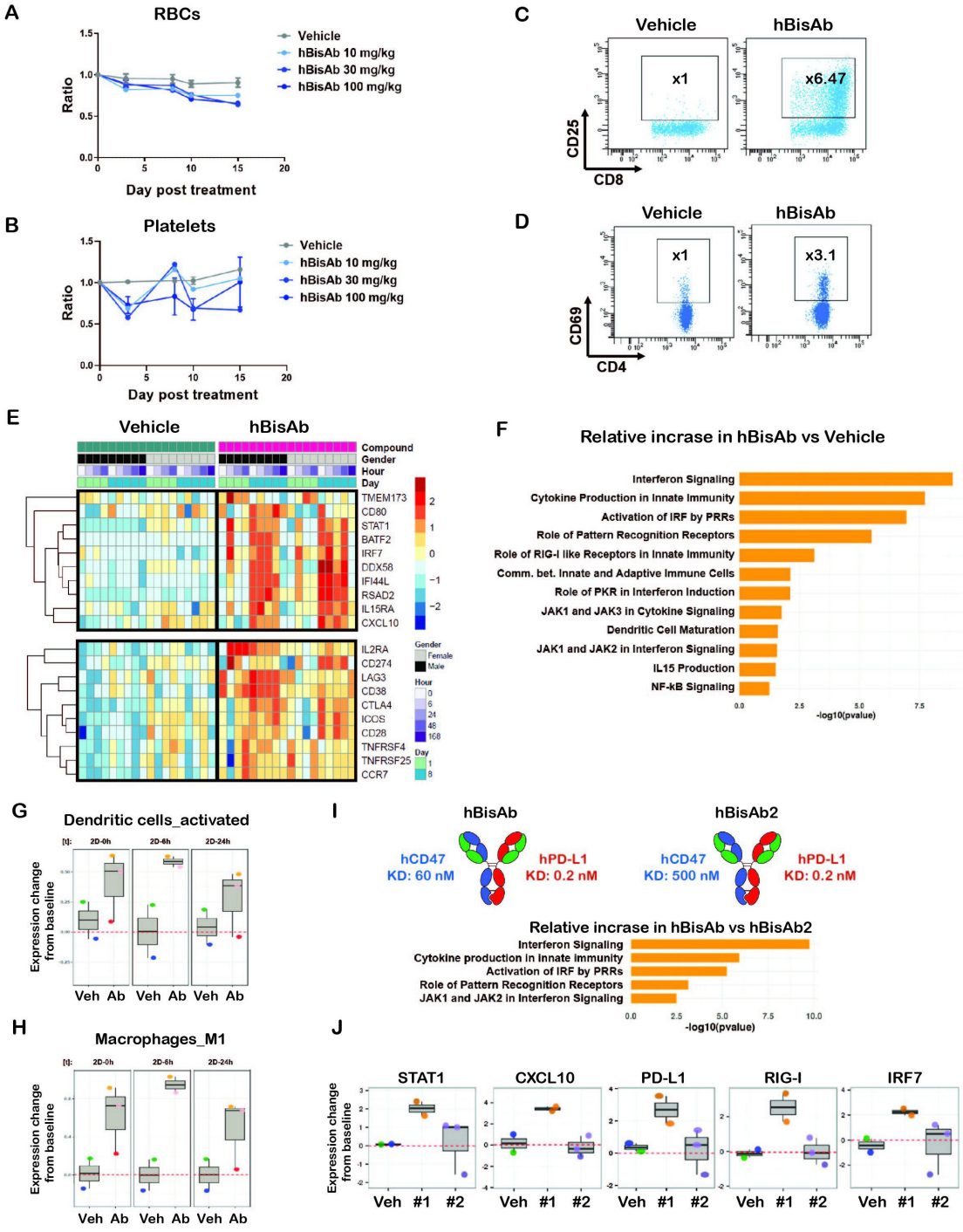

Figure 7 Non-human primate study with human αCD47/PD-L1 bispecific antibody (hBisAb) treatment. (A, B) Cynomolgus monkeys received vehicle control and 10, 30, and 100 mg/kg of hBisAb on day 1 and 8 (n=1–3 monkey/group). The peripheral blood was collected at the indicated timepoint for RBC (A) and platelet numbers (B) in response to the treatment. Ordinary one-way ANOVA with Dunnett's multiple comparisons test. (C, D) Representative flow cytometry plots of $CD25^+$ $CD4^+$ and $CD69^+$ $CD8^+$ T cell populations from NHP peripheral blood on day 8 after receiving vehicle control or 100 mg/kg of hBisAb. (E–H) The NHP PBMCs from peripheral blood were collected with the indicated timepoints after receiving vehicle control or 100 mg/kg of hBisAb on day 1 and 8 for RNA-seq analysis (n=2–3 monkey/group). (E) Selected DEGs associated with innate and adaptive immune pathways in vehicle-treated versus hBisAb-treated samples across all the timepoints during a 2-week period. (F) IPA pathway analysis of the RNA-seq from hBisAb-treated compared with vehicle-treated group on 6 hours post-second dose on day 8. (G, H) LM22 gene signature scores (relative to baseline) of activated DCs and M1 macrophages in vehicle (Veh) vs hBisAb (Ab)-treated group on 0, 6, and 24 hours post-second dose (2D). (I, J) The peripheral blood from cyno received 100 mg/kg of hBisAb and hBisAb2 with reduced CD47 affinity on day 1 and 8 (n=2–3 monkey/group) was collected for RNA-seq analysis. The molecule affinity and enriched IPA pathway scores (I) as well as the selected DEGs (J) expression profiles are listed for the comparison of the two antibodies. 2D, two dimensional; ANOVA, analysis of variance; DC, dendritic cell; DEG, differentially expressed gene; NHP, non-human primate; PBMC, peripheral blood mononuclear cell; RBC, red blood cell.

PD-L1 bispecific antibodies in NHP and murine systems showed minimal anemia but maintained strong innate and adaptive immune responses. Finally, we identified unique myeloid and T cell activation patterns following the bispecific treatment in murine and NHP systems, demonstrating its potent ability to engage both innate and adaptive immune responses for antitumor efficacy.

Our comparative gene expression analysis revealed that distinct from αCD47 and αPD-L1 monotherapies or combination therapies, mBisAb-treated tumor tissues displayed robust upregulation in pathways associated with innate activation, including PRR-mediated induction of IFNα pathways, type I IFN signaling, and FcγR dependent phagocytosis. PRR signaling, including activation of STING by sensing of cytosolic dsDNA, can promote type I IFN and other proinflammatory cytokine production in DCs and TAMs by inducing the nuclear translocation and activity of transcription factors NF-kB and IRF3/7.[17 40–44] Indeed, recent research utilizing IFNAR$^{-/-}$ and STING$^{-/-}$ mouse models highlight the necessity of these pathways in mediating CD47 blockade-induced tumor rejection by enhanced innate sensing of tumor cells via cGAS-STING signaling, leading to enhanced cross-priming of CD8 T cells.[14 18] Our data indicate that both innate and adaptive responses are necessary for mBisAb efficacy, in concordance with previous work co-targeting the CD47/SIRPα and PD-1/PD-L1 axis in preclinical tumor models.[14 45 46] However, how myeloid and T cells are modulated transcriptionally at the single-cell level has not been extensively evaluated in the previous studies. Our scRNA-seq data revealed an upregulation in the expression of genes associated with a response to type I IFN within intratumoral cDC1 cells. cDC2, which coexpress PD-L1 and SIRPα and may be directly impacted by mBisAb therapy, instead displayed an increase in the relative expression of genes associated with antigen processing and presentation. Increased antigen processing and presentation were also observed within mregDCs, a population particularly enriched for PD-L1 expression and associated with an immunosuppressive phenotype,[24] suggesting possible reprogramming of this population by mBisAb targeting.

In addition to impacts on DC populations, our scRNA-seq analysis of TAM clusters also revealed a dramatic increase in gene expression associated with antigen processing and presentation and a downregulation of genes associated with cell cycle following mBisAb treatment. Notably, this signature is consistent with exposure to IFNγ[47 48] and may in part be explained by the expansion of IFNγ producing CD8$^+$ T cell population following mBisAb treatment. Indeed, TAM repolarization following αPD-(L)1 treatment is mediated mainly by increased IFNγ signaling and required IFNγR expression on TAMs.[48] Furthermore, type I IFN sensitizes TAMs to IFNγ through increased STAT1 signaling,[49] which gene signature was enriched in mBisAb-treated tumor tissues. Interestingly, the combination of monotherapies similarly induced the relative loss of cell cycle-specific transcripts but did not increase antigen processing and presentation genes, suggesting that mBisAb may be more efficient at targeting or activating these TAM populations. Our data support a model in which BisAb treatment activates innate immunity to stimulate adaptive responses within the TME, which may in turn act to repolarize TAM populations further to support antitumor immunity.

Previous studies have demonstrated enhanced cross-priming and activation of tumor antigen-specific CD8$^+$ T cells by DCs and macrophages following SIRPα-CD47 pathway blockade.[17 18 50] However, the impact of SIRPα-CD47 pathway inhibition on the size and distribution of intratumoral CD8$^+$ T cell populations remained unknown. Here, we found that mBisAb treatment induced robust expansion of the intratumoral CD8$^+$ T cell pool in vivo. Notably, populations that have been positively correlated with patient responsiveness to checkpoint blockade therapy, including the Tcf1$^+$ stem-like progenitor[26–28] and effector-like CD8$^+$ T cells, were more significantly expanded by mBisAb than αPD-L1 or its combination with αCD47. In addition to the robust expansion of the Tcf1$^+$ stem-like progenitor population, mBisAb also induced its differentiation into an effector-like state. Furthermore, mBisAb treatment resulted in the most significant expansion of an effector-like CD8$^+$ T cell population characterized by high expression of *Ifng* that was transcriptionally distinct from the terminally exhausted T cell population. Notably, a recent study demonstrated that a signature of activation and differentiation among the intratumoral Tcf1$^+$ stem-like progenitor CD8$^+$ T cell population was a hallmark of patients successfully responding to immune checkpoint blockade (ICB).[51] Moreover, signatures related to T cell cytolytic activity and IFNγ signaling, which include genes highly expressed by the effector-like CD8$^+$ T cell population (*Ifng*, *Prf1*) that was robustly expanded by mBisAb treatment, have also been correlated with patient responsiveness to ICB therapy.[37 39] Taken together, these findings suggest that mBisAb treatment successfully induces an intratumoral CD8$^+$ T cell landscape highly reflective of patients undergoing an effective response to ICB therapy by both expanding the Tcf1$^+$ stem-like progenitor population and promoting its differentiation to an effector-like state.

PD-1/PD-L1 pathway blockade is known to expand the Tcf1$^+$ stem-like progenitor population,[26 27] but the exact mechanism by which mBisAb expands this population further remains unclear. However, one likely explanation is that enhanced cross-priming by intratumoral APCs mediated by CD47 blockade[17 18] could further bolster the expansion of the Tcf1$^+$ stem-like progenitor population mediated by PD-L1 blockade. Indeed, an increased gene expression signature related to antigen processing and presentation following mBisAb treatment and loss of mBisAb-mediated efficacy in Batf3$^{-/-}$ mice both indicate that DCs may play a vital role in the stem-like progenitor CD8$^+$ T cell expansion. Given the enhanced binding selectivity of the αCD47/PD-L1 BisAb to the TME relative

to αCD47, an increase in antibody exposure for sufficient SIRPα-CD47 blockade within the TME could explain the expansion of the Tcf1$^+$ stem-like and effector-like CD8$^+$ T cell populations in response to mBisAb relative to αPD-L1 and its combination with αCD47. A recent study has demonstrated that Tcf1$^+$ stem-like progenitor CD8$^+$ T cells reside primarily within APC-rich niches within the TME.[52] Robust activation of APCs by BisAb-mediated tumor-directed SIRPα-CD47 pathway blockade could help create such niches that could support the persistence and/or differentiation of the Tcf1$^+$ stem-like progenitor population further to its expansion by the PD-L1 arm. Taken together, these findings indicate that targeting both innate and adaptive checkpoints using a bispecific approach can synergistically remodel the intratumoral immune landscape to a state that promotes potent anti-tumor activity. Our findings suggest that this therapeutic approach holds promising potential to improve patient outcomes over current PD-(L)1 and CD47-targeted therapies.

Acknowledgements The authors thank Robert Rickert, Premal Patel, and Barbra Sasu for their useful discussions. The authors also thank Cindy Li, Breanna Jung, Pamela Santiago, Sophanna Kong, Parul Gupta, Jatin Narula, Qinghai Peng, Qing Zong, Jianying Wang, Vicki Markiewicz, Guoyun Zhu, Christopher Dillon, Eleanore Hendrickson, Lynn Wang, Nancy Chau, Muamera Zulcic, Rupesh Kanchi Ravi, Xianxian Zheng, Jennifer Kinong, David Schaer, Dirk Zajonc, James Patterson, Chiu Lau-Barre, Matthew Kunicki, Allison Vitsky, Yvonne S. L. Mak, Sindy Liao Chan, Tina Mistry, Colleen L. Brown, Sherman M. Chin, Joanna Ngo, James Apgar, Daniel McDonough, Willie Wang, Tao Sai and Xi Yang for technical assistance or guidance.

Contributors S-HC, PKD, JS, SD, JC-R, and SS-A led the design of the molecule and experiments. S-HC, PKD, JS, NK, RL, and JH performed experiments, analysed data, interpret the data, and wrote the manuscript. CW, ZM, TVB, and KCL assisted with design of the molecule, conducting, and interpretation of the experiments. WY, S-HC, NK, and RL assisted with design of the computational methods and/or with interpretation of the analyses. S-HC, JC-R, and SS-A led the design, interpretation, and the editing of the manuscript.

Funding This study was funded by Pfizer.

Competing interests All authors are employees of Pfizer which developed antibodies presented in this manuscript.

Patient consent for publication Not required.

Ethics approval All animal experiments were approved by the Institutional Animal Use and Care Committee of Pfizer and in compliance with the Animal Welfare Act, the Guide for the Care and Use of Laboratory Animals, and the Office of Laboratory Animal Welfare.

Provenance and peer review Not commissioned; externally peer reviewed.

Data availability statement All data are available in the main text or the online supplemental materials. The accession number for the mouse and NHP RNA-seq data is GSE177053. Requests for materials should be directed to and will be fulfilled by S-HC, JC-R, or SS-A and the completion of a material transfer agreement with Pfizer.

ORCID iDs
Shih-Hsun Chen http://orcid.org/0000-0002-0412-273X
Shahram Salek-Ardakani http://orcid.org/0000-0002-2336-8452

REFERENCES

1 Topalian SL, Drake CG, Pardoll DM. Immune checkpoint blockade: a common denominator approach to cancer therapy. *Cancer Cell* 2015;27:450–61.
2 Egen JG, Ouyang W, Wu LC. Human anti-tumor immunity: insights from immunotherapy clinical trials. *Immunity* 2020;52:36–54.
3 Willingham SB, Volkmer J-P, Gentles AJ, *et al*. The CD47-signal regulatory protein alpha (SIRPa) interaction is a therapeutic target for human solid tumors. *Proc Natl Acad Sci U S A* 2012;109:6662–7.
4 Logtenberg MEW, Scheeren FA, Schumacher TN. The CD47-SIRPα immune checkpoint. *Immunity* 2020;52:742–52.
5 Oldenborg P-A. Cd47: a cell surface glycoprotein which regulates multiple functions of hematopoietic cells in health and disease. *ISRN Hematol* 2013;2013:614619
6 Matlung HL, Szilagyi K, Barclay NA, *et al*. The CD47-SIRPα signaling axis as an innate immune checkpoint in cancer. *Immunol Rev* 2017;276:145–64.
7 Casey SC, Tong L, Li Y, *et al*. MYC regulates the antitumor immune response through CD47 and PD-L1. *Science* 2016;352:227–31.
8 Manguso RT, Pope HW, Zimmer MD, *et al*. In vivo CRISPR screening identifies PTPN2 as a cancer immunotherapy target. *Nature* 2017;547:413–8.
9 Lakhani NJ, Patnaik A, Liao JB, *et al*. A phase Ib study of the anti-CD47 antibody magrolimab with the PD-L1 inhibitor avelumab (a) in solid tumor (ST) and ovarian cancer (OC) patients. *JCO* 2020;38:18.
10 Chao MP, Takimoto CH, Feng DD, *et al*. Therapeutic targeting of the macrophage immune checkpoint CD47 in myeloid malignancies. *Front Oncol* 2019;9:1380.
11 Advani R, Flinn I, Popplewell L, *et al*. CD47 blockade by Hu5F9-G4 and rituximab in non-Hodgkin's lymphoma. *N Engl J Med* 2018;379:1711–21.
12 Sikic BI, Lakhani N, Patnaik A, *et al*. First-In-Human, first-in-class phase I trial of the Anti-CD47 antibody Hu5F9-G4 in patients with advanced cancers. *J Clin Oncol* 2019;37:946–53.
13 Van Blarcom T, Lindquist K, Melton Z, *et al*. Productive common light chain libraries yield diverse panels of high affinity bispecific antibodies. *MAbs* 2018;10:256–68.
14 Liu X, Liu L, Ren Z, *et al*. Dual targeting of innate and adaptive checkpoints on tumor cells limits immune evasion. *Cell Rep* 2018;24:2101–11.
15 Sockolosky JT, Dougan M, Ingram JR, *et al*. Durable antitumor responses to CD47 blockade require adaptive immune stimulation. *Proc Natl Acad Sci U S A* 2016;113:E2646–54.
16 Ataide MA, Komander K, Knöpper K, *et al*. BATF3 programs CD8+ T cell memory. *Nat Immunol* 2020;21:1397–407.
17 Xu MM, Pu Y, Han D, *et al*. Dendritic cells but not macrophages sense tumor mitochondrial DNA for cross-priming through signal regulatory protein α signaling. *Immunity* 2017;47:363–73.
18 Liu X, Pu Y, Cron K, *et al*. CD47 blockade triggers T cell-mediated destruction of immunogenic tumors. *Nat Med* 2015;21:1209–15.
19 Wei SC, Levine JH, Cogdill AP, *et al*. Distinct cellular mechanisms underlie anti-CTLA-4 and anti-PD-1 checkpoint blockade. *Cell* 2017;170:e1117:1120–33.
20 Quezada SA, Peggs KS, Curran MA, *et al*. CTLA4 blockade and GM-CSF combination immunotherapy alters the intratumor balance of effector and regulatory T cells. *J Clin Invest* 2006;116:1935–45.
21 Sato E, Olson SH, Ahn J, *et al*. Intraepithelial CD8+ tumor-infiltrating lymphocytes and a high CD8+/regulatory T cell ratio are associated with favorable prognosis in ovarian cancer. *Proc Natl Acad Sci U S A* 2005;102:18538–43.
22 Mariathasan S, Turley SJ, Nickles D, *et al*. Tgfβ attenuates tumour response to PD-L1 blockade by contributing to exclusion of T cells. *Nature* 2018;554:544–8.
23 Zilionis R, Engblom C, Pfirschke C, *et al*. Single-cell transcriptomics of human and mouse lung cancers reveals conserved myeloid populations across individuals and species. *Immunity* 2019;50:1317–34.
24 Maier B, Leader AM, Chen ST, *et al*. A conserved dendritic-cell regulatory program limits antitumour immunity. *Nature* 2020;580:257–62.

25 Peng Q, Qiu X, Zhang Z, *et al*. PD-L1 on dendritic cells attenuates T cell activation and regulates response to immune checkpoint blockade. *Nat Commun* 2020;11:4835.
26 Siddiqui I, Schaeuble K, Chennupati V, *et al*. Intratumoral Tcf1^{+}PD-1^{+}CD8^{+} T cells with stem-like properties promote tumor control in response to vaccination and checkpoint blockade immunotherapy. *Immunity* 2019;50:195–211.
27 Miller BC, Sen DR, Al Abosy R, *et al*. Subsets of exhausted CD8^{+} T cells differentially mediate tumor control and respond to checkpoint blockade. *Nat Immunol* 2019;20:326–36.
28 Sade-Feldman M, Yizhak K, Bjorgaard SL, *et al*. Defining T cell states associated with response to checkpoint immunotherapy in melanoma. *Cell* 2018;175:e1020:998–1013.
29 Ntanasis-Stathopoulos I, Fotiou D, Terpos E. CCL3 signaling in the tumor microenvironment. *Adv Exp Med Biol* 2020;1231:13–21.
30 Williford J-M, Ishihara J, Ishihara A, *et al*. Recruitment of CD103^{+} dendritic cells via tumor-targeted chemokine delivery enhances efficacy of checkpoint inhibitor immunotherapy. *Sci Adv* 2019;5:eaay1357.
31 Zander R, Schauder D, Xin G, *et al*. CD4^{+} T Cell Help Is Required for the Formation of a Cytolytic CD8^{+} T Cell Subset that Protects against Chronic Infection and Cancer. *Immunity* 2019;51:1028–42.
32 Hudson WH, Gensheimer J, Hashimoto M, *et al*. Proliferating Transitory T Cells with an Effector-like Transcriptional Signature Emerge from PD-1^{+} Stem-like CD8^{+} T Cells during Chronic Infection. *Immunity* 2019;51:1043–58.
33 Yamauchi T, Hoki T, Oba T, *et al*. T-cell CX3CR1 expression as a dynamic blood-based biomarker of response to immune checkpoint inhibitors. *Nat Commun* 2021;12:1402.
34 Yan Y, Cao S, Liu X, *et al*. CX3CR1 identifies PD-1 therapy-responsive CD8+ T cells that withstand chemotherapy during cancer chemoimmunotherapy. *JCI Insight* 2018;3:1. doi:10.1172/jci.insight.97828
35 Celis-Gutierrez J, Blattmann P, Zhai Y, *et al*. Quantitative interactomics in primary T cells provides a rationale for concomitant PD-1 and BTLA coinhibitor blockade in cancer immunotherapy. *Cell Rep* 2019;27:3315–30.
36 Kaech SM, Hemby S, Kersh E, *et al*. Molecular and functional profiling of memory CD8 T cell differentiation. *Cell* 2002;111:837–51.
37 Riaz N, Havel JJ, Makarov V, *et al*. Tumor and microenvironment evolution during immunotherapy with nivolumab. *Cell* 2017;171:934–49.
38 Zemek RM, De Jong E, Chin WL, *et al*. Sensitization to immune checkpoint blockade through activation of a STAT1/NK axis in the tumor microenvironment. *Sci Transl Med* 2019;11 doi:10.1126/scitranslmed.aav7816
39 Ayers M, Lunceford J, Nebozhyn M, *et al*. IFN-γ-related mRNA profile predicts clinical response to PD-1 blockade. *J Clin Invest* 2017;127:2930–40.
40 Kaczanowska S, Joseph AM, Davila E. TLR agonists: our best frenemy in cancer immunotherapy. *J Leukoc Biol* 2013;93:847–63.
41 Sabroe I, Parker LC, Dower SK, *et al*. The role of TLR activation in inflammation. *J Pathol* 2008;214:126–35.
42 Sun L, Wu J, Du F, *et al*. Cyclic GMP-AMP synthase is a cytosolic DNA sensor that activates the type I interferon pathway. *Science* 2013;339:786–91.
43 Li D, Wu R, Guo W, *et al*. STING-mediated IFI16 degradation negatively controls type I interferon production. *Cell Rep* 2019;29:1249–60.
44 Cunha LD, Yang M, Carter R, *et al*. LC3-associated phagocytosis in myeloid cells promotes tumor immune tolerance. *Cell* 2018;175:429–41.
45 Liu B, Guo H, Xu J, *et al*. Elimination of tumor by CD47/PD-L1 dual-targeting fusion protein that engages innate and adaptive immune responses. *MAbs* 2018;10:315–24.
46 Wang Y, Ni H, Zhou S, *et al*. Tumor-selective blockade of CD47 signaling with a CD47/PD-L1 bispecific antibody for enhanced anti-tumor activity and limited toxicity. *Cancer Immunol Immunother* 2021;70:365–76.
47 Dangaj D, Bruand M, Grimm AJ, *et al*. Cooperation between constitutive and inducible chemokines enables T cell engraftment and immune attack in solid tumors. *Cancer Cell* 2019;35:885–900.
48 Xiong H, Mittman S, Rodriguez R, *et al*. Anti-PD-L1 treatment results in functional remodeling of the macrophage compartment. *Cancer Res* 2019;79:1493–506.
49 Karonitsch T, von Dalwigk K, Steiner CW, *et al*. Interferon signals and monocytic sensitization of the interferon-γ signaling pathway in the peripheral blood of patients with rheumatoid arthritis. *Arthritis Rheum* 2012;64:400–8.
50 Tseng D, Volkmer J-P, Willingham SB, *et al*. Anti-CD47 antibody-mediated phagocytosis of cancer by macrophages primes an effective antitumor T-cell response. *Proc Natl Acad Sci U S A* 2013;110:11103–8.
51 Bi K, He MX, Bakouny Z, *et al*. Tumor and immune reprogramming during immunotherapy in advanced renal cell carcinoma. *Cancer Cell* 2021;39:649–61.
52 Jansen CS, Prokhnevska N, Master VA, *et al*. An intra-tumoral niche maintains and differentiates stem-like CD8 T cells. *Nature* 2019;576:465–70.

Supplementary Information for

Dual checkpoint blockade of CD47 and PD-L1 using an affinity-tuned bispecific antibody maximizes anti-tumor immunity

Chen S-H, *et al. J Immunother Cancer* 2021; 9:e003464. doi: 10.1136/jitc-2021-003464

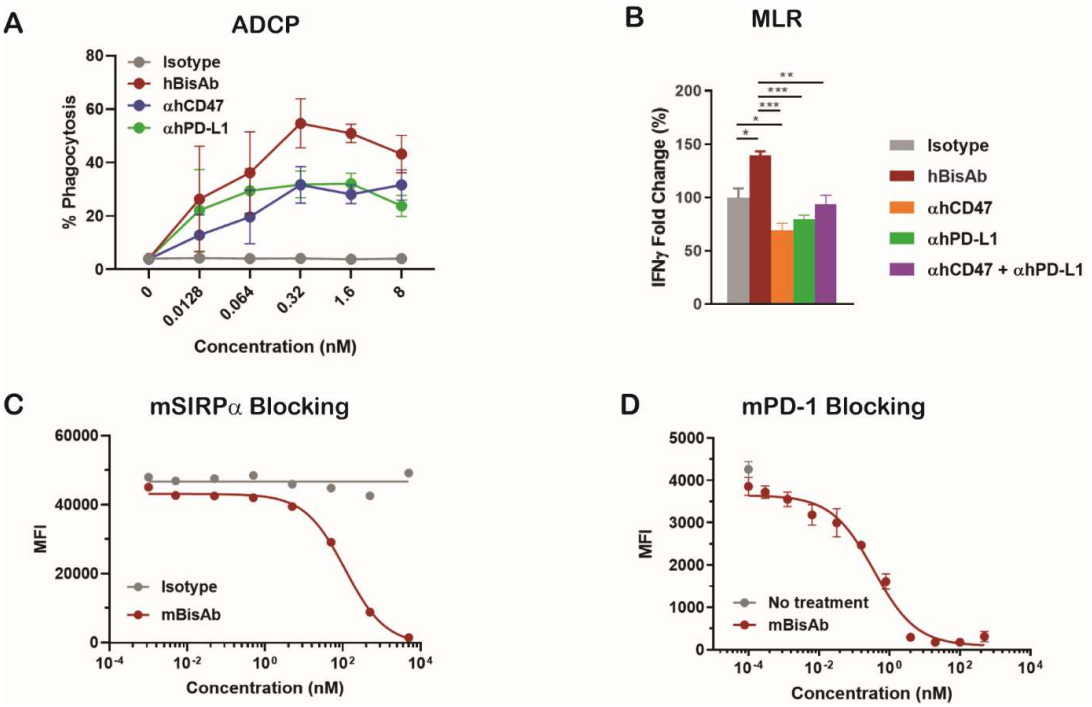

Supplementary Figure 1. ***In vitro*** **functionality of hBisAb and mBisAb** (**A**) Phagocytosis of NCI-H292 tumor cells by human macrophages in the presence of human IgG1 isotype controls, hBisAb, αhCD47, and αhPD-L1. A mixture of CFSE labeled tumor cells and CTV labeled macrophages were co-cultured at a 1:2 ratio for 2 hours with increasing concentrations the antibodies and analyzed by flow cytometry. Phagocytosis of total tumor cells is represented as fold change compared to isotype treatment. (**B**) MLR was conducted to assess concentration of IFNγ at 120 hours in the supernatant by ELISA. A mixture of LPS matured DCs and purified $CD4^+$ T cells were co-cultured at a 1:4 ratio with 200 nM of isotype control, hBisAb, αhCD47, αhPD-L1, or combination treatment of αhCD47 and αhPD-L1 at same molar ratio. *p<0.05, **p<0.01, ***p<0.001, One-way ANOVA. (**C**) *In vitro* blocking activity of mBisAb on the mouse CD47/SIRPα interaction as measured by flow cytometry. (**D**) *In vitro* blocking activity of mBisAb on the mouse PD-L1/PD-1 interaction as measured by flow cytometry.

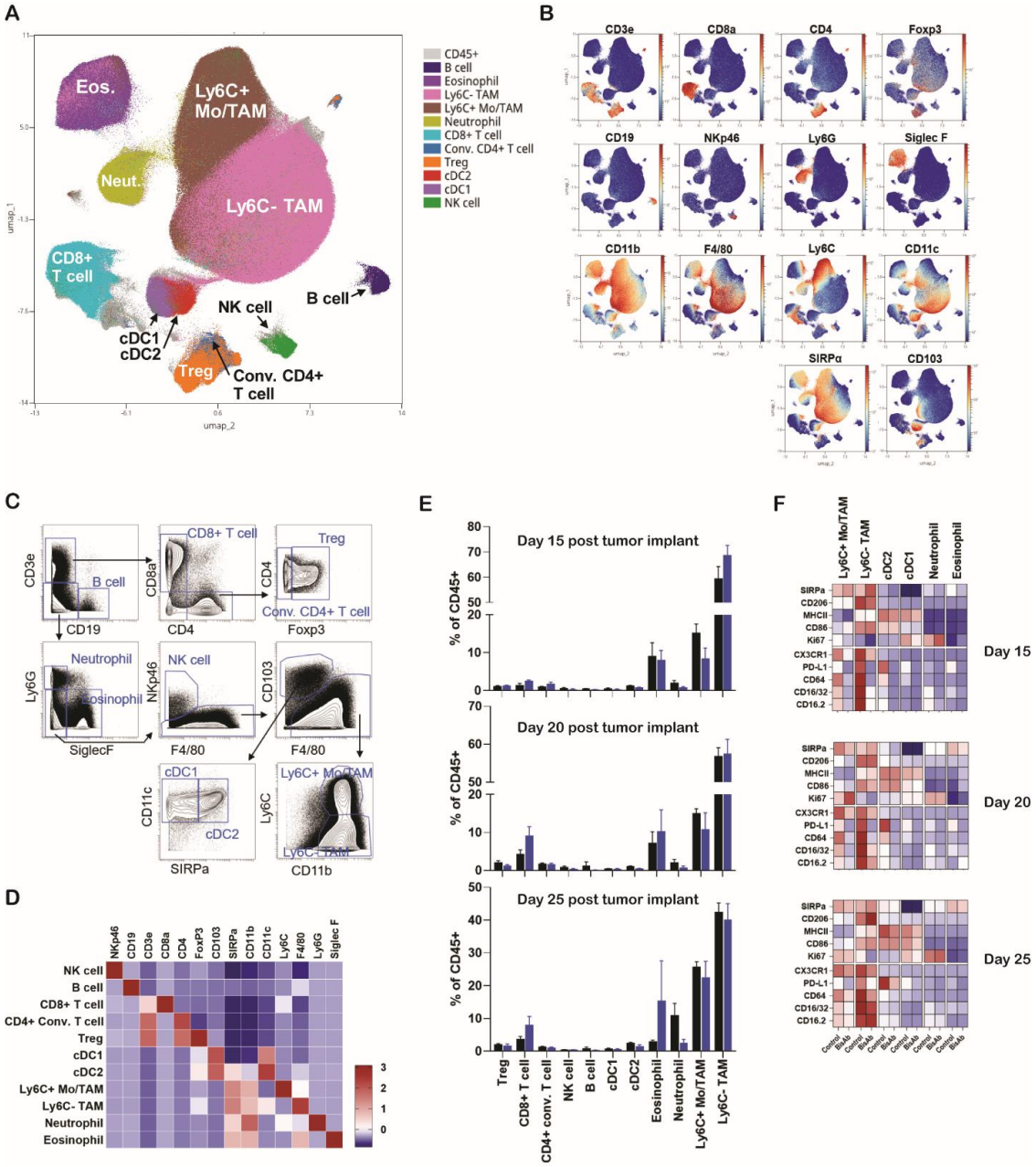

Supplementary Figure 2. Designation of intratumoral immune cell population by CyTOF

(**A-F**) The same samples of MC38 tumors and spleens in Figure 4A-F were further analyzed by CyTOF. (**A**) UMAP plot of total intratumoral CD45^{+} cells. Populations identified via biaxial gating are overlaid. (**B**) Single-cell expression of lineage markers used to define major leukocyte

populations. (**C**) Identification of major leukocyte populations via biaxial gating. (**D**) Relative expression of lineage markers within major leukocyte populations. (**E**) Frequency of leukocyte populations among total $CD45^+$ cells in control (black) or mBisAb-treated (blue) tumors at the indicated timepoints post-first dose of treatment. (**F**) Relative expression of activation markers within myeloid populations in control or mBisAb-treated tumors at the indicated timepoints post-tumor implantation.

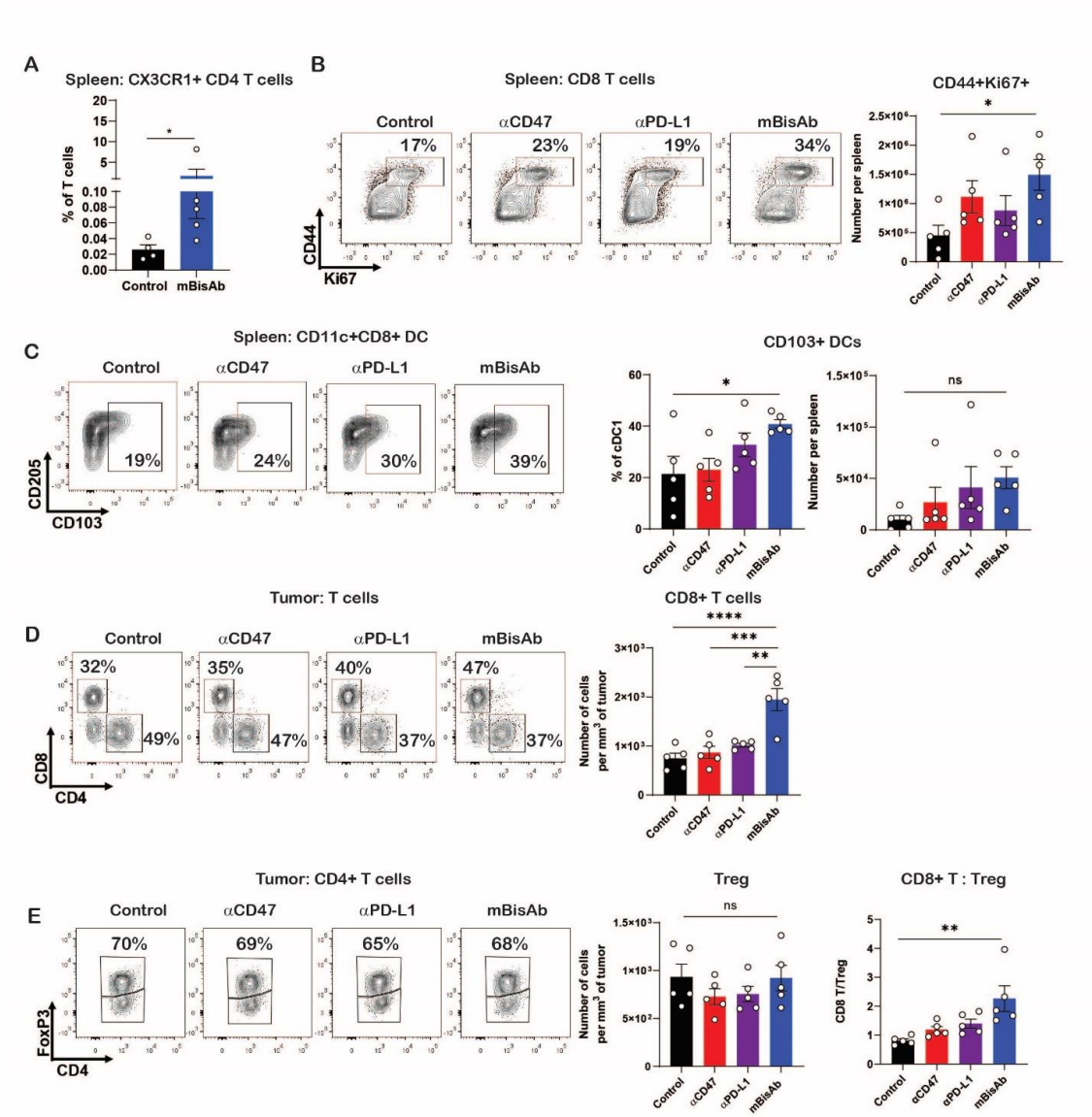

Supplementary Figure 3. Flow cytometric characterization of intratumoral and splenic immune populations in mBisAb-treated mice (**A**) Mice were treated as described in Figure 4. Frequency of $CD44^{hi}CD62L^{lo}CX3CR1^{+}PD\text{-}1^{+}FoxP3^{-}CD4^{+}$ T cells among total T cells in the spleens of control (black) or mBisAb-treated (blue) mice at day 20 post-implantation as determined by CyTOF analysis. *P<0.05, Mann Whitney test.(**B-E**) MC38-bearing mice were treated with isotype (control, black), αmCD47 (red), αmPD-L1(purple), or mBisAb (blue) every 3 to 4 days

starting at day 10 post-tumor implantation. Tumors and spleens were then harvested at day 20 for flow cytometric analysis (*n*=5 mice/group). (**B**) Quantification of activated proliferating ($CD44^+Ki67^+$) CD8 T cells in the spleens of mice with each indicated treatment, with representative flow cytometry plots shown to the left. (**C**) Frequency of $CD103^+$ cells within cDC1 and quantification of $CD103^+$ DCs in the spleens of mice with indicated treatments, with representative flow cytometry plots shown to the left. (**D**) Quantification of total CD8 T cells in the tumors of mice with the indicated treatments, with representative flow cytometry plots shown to the left. (**E**) Quantification of total Tregs ($CD4^+FoxP3^+$ T cells) in the tumors of mice with the indicated treatments, and ratio of the total number of $CD8^+$ T cells relative to the total number of Tregs in each tumor, with representative gating of Tregs shown to the left. ns P>0.05, *P<0.05, **P<0.01, ***P<0.001, ****P<0.0001, One-way ANOVA with multiple comparisons.

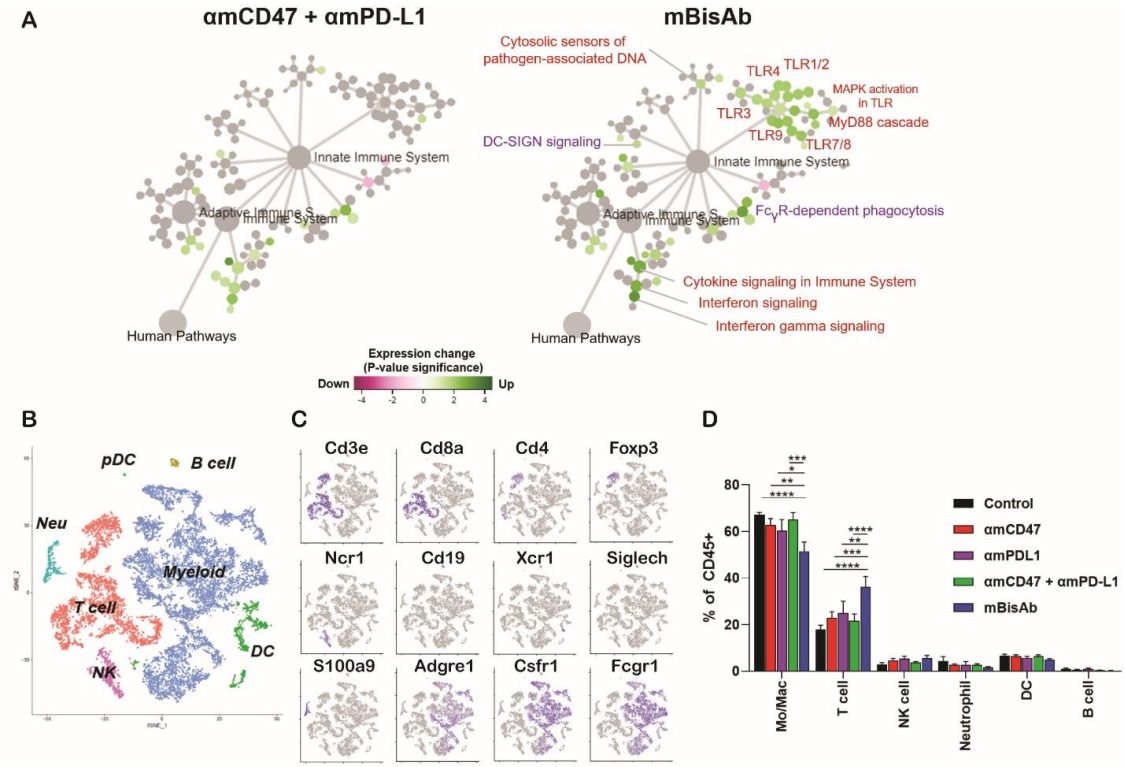

Supplementary Figure 4. Pathway analysis by Nanostring and designation of immune cell populations by scRNA-seq (**A**) Pathway correlation network analysis on the samples in mBisAb-treated group compared with the αmCD47 and αmPD-L1 combination group in Figure 5A. (**B-D**) Analysis of scRNA-seq samples in Figure 5. (**B**) tSNE analysis of intratumoral $CD45^+$ cells from across all treatment conditions, with cell lineages overlaid. (**C**) Single-cell expression of representative lineage markers used to designate major leukocyte populations. (**D**) Frequency of each lineage among total $CD45^+$ cells in each treatment condition. *P<0.05, **P<0.01, ***P<0.001, ***P<0.0001, two-way ANOVA with tukey's multiple comparison test.

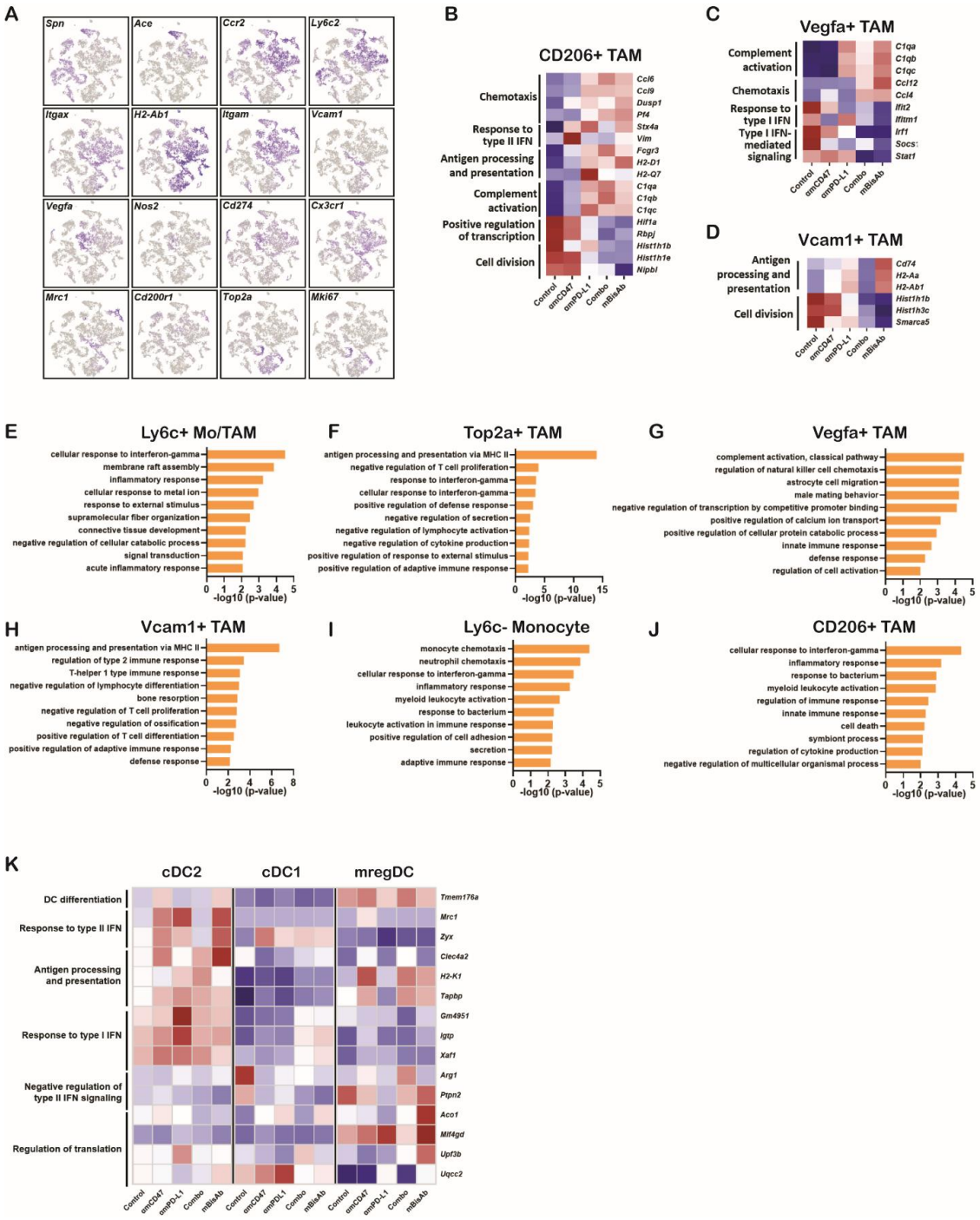

Supplementary Figure 5. scRNA-seq analysis on myeloid and DC clusters following mBisAb treatment (**A**) Single-cell expression of representative markers used to characterize intratumoral

monocyte and macrophage populations. (**B-D**) Relative average expression across treatment groups for selected genes that are differentially expressed among the indicated clusters in mBisAb- versus control-treated tumors. (**E-J**) Selected hits from GO pathway analysis performed on genes differentially expressed by the indicated clusters from mBisAb-treated tumors relative to controls. (**K**) Selected DEGs for DC clusters in mBisAb- versus control-treated tumors. Expression is displayed relative to all treatment groups and clusters.

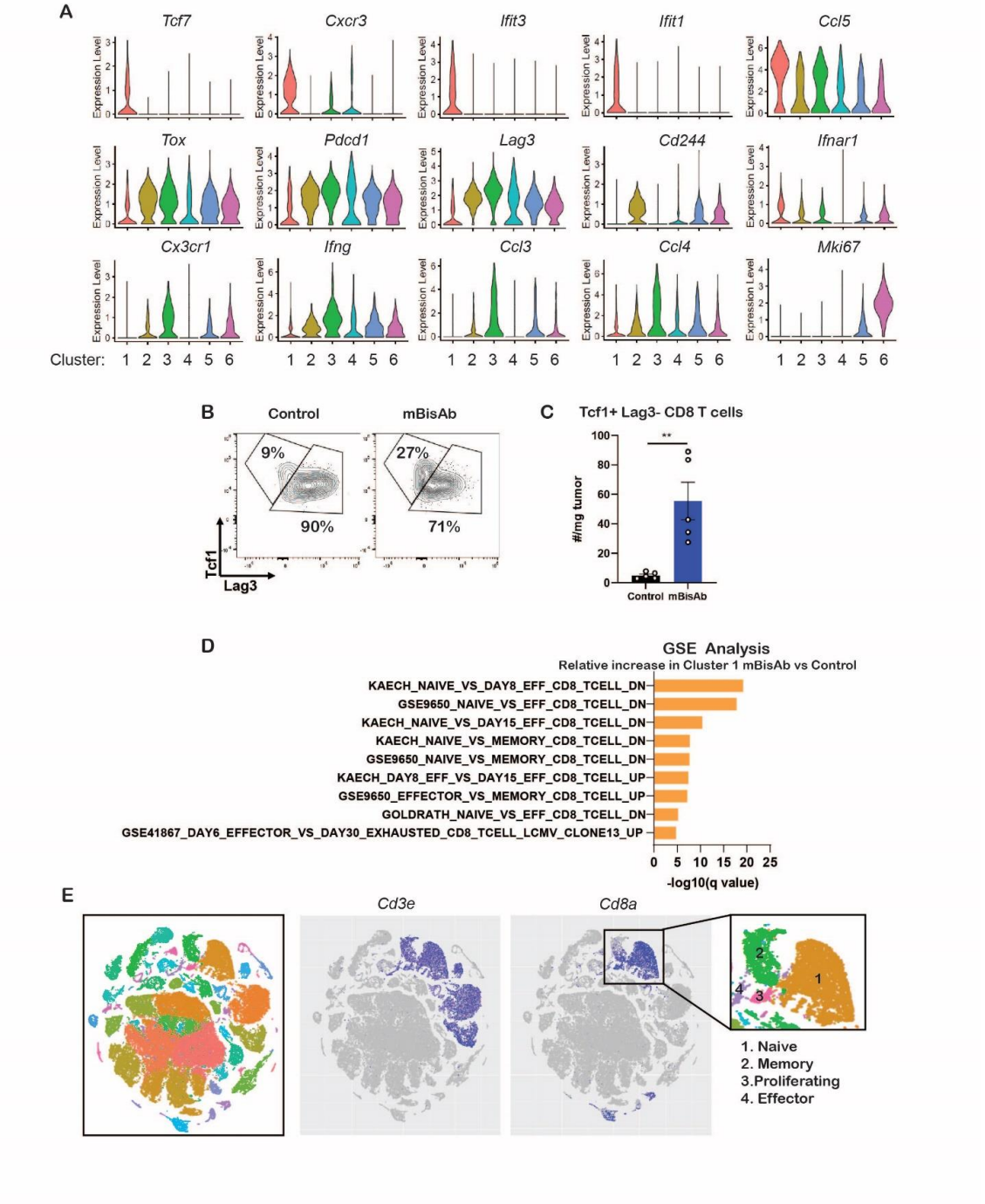
A
Tcf7
Cxcr3
Ifit3
Ifit1
Ccl5
Tox
Pdcd1
Lag3
Cd244
Ifnar1
Cx3cr1
Ifng
Ccl3
Ccl4
Mki67
Expression Level
Cluster: 1 2 3 4 5 6
B
Control
mBisAb
9%
90%
27%
71%
Tcf1
Lag3
C
Tcf1+ Lag3- CD8 T cells
#/mg tumor
Control
mBisAb
D
GSE Analysis
Relative increase in Cluster 1 mBisAb vs Control
KAECH_NAIVE_VS_DAY8_EFF_CD8_TCELL_DN
GSE9650_NAIVE_VS_EFF_CD8_TCELL_DN
KAECH_NAIVE_VS_DAY15_EFF_CD8_TCELL_DN
KAECH_NAIVE_VS_MEMORY_CD8_TCELL_DN
GSE9650_NAIVE_VS_MEMORY_CD8_TCELL_DN
KAECH_DAY8_EFF_VS_DAY15_EFF_CD8_TCELL_UP
GSE9650_EFFECTOR_VS_MEMORY_CD8_TCELL_UP
GOLDRATH_NAIVE_VS_EFF_CD8_TCELL_DN
GSE41867_DAY6_EFFECTOR_VS_DAY30_EXHAUSTED_CD8_TCELL_LCMV_CLONE13_UP
-log10(q value)
E
Cd3e
Cd8a
1. Naive
2. Memory
3.Proliferating
4. Effector

Supplementary Figure 6. scRNA-seq analysis of CD8 T cell populations in the tumor and spleen following mBisAb treatment (**A**) Violin plots depicting normalized and log-transformed single-cell expression (logTPM, transcripts per million) of selected genes across CD8 T cell clusters. (**B,C**) Mice were treated as in Figure 6 and tumors were harvested at the same time points for flow cytometric analysis (n=5 mice/group). (**B**) Representative flow cytometry plots of $Tcf1^{hi}$ $Lag3^{lo}$ versus $Tcf1^{lo}$ $Lag3^{hi}$ populations among antigen-experienced ($CD44^{hi}CD62L^{lo}$) intratumoral CD8 T cells in control versus mBisAb-treated tumors. (**C**) Total numbers of $CD44^{hi}CD62L^{lo}$ $Tcf1^{hi}$ $Lag3^{lo}$ intratumoral CD8 T cells in control versus mBisAb-treated tumors. **P<0.01, Student's unpaired T-test. (**D**) Selected hits from gene set enrichment (GSE) analysis performed on genes differentially expressed by Cluster 1 intratumoral CD8 T cells from BisAb-treated relative to control-treated mice. (**E**) tSNE analysis of splenic $CD45^{+}$ cells from across all treatment conditions, with superimposed single-cell expression patterns of *Cd3e* and *Cd8a*, where each cell is colored according to the TPM value. Inset shows CD8 T cell clusters as determined by gene expression patterns in Figure 6G.

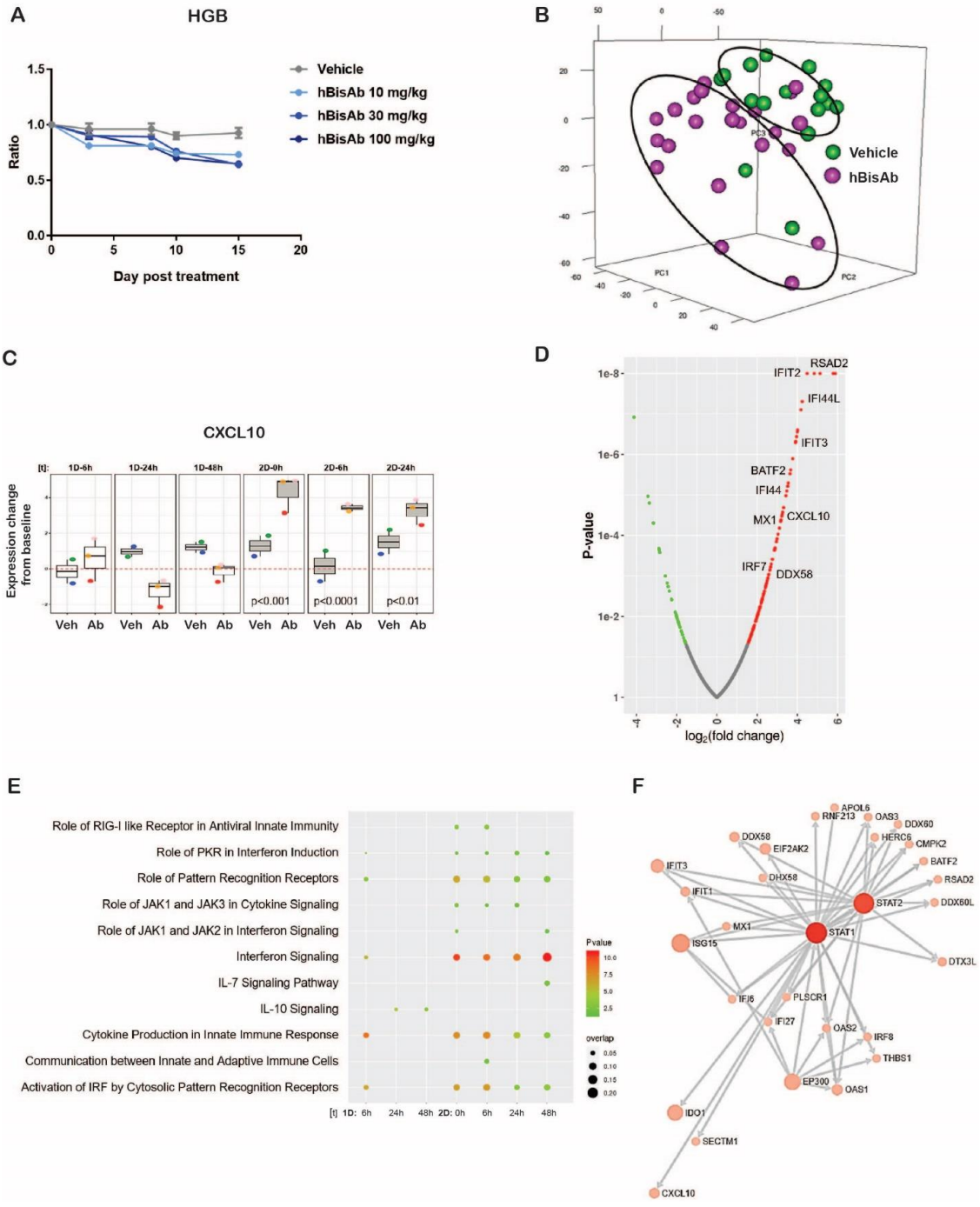

Supplementary Figure 7. Hemoglobin and gene expression analysis in NHP peripheral blood following hBisAb treatment (**A**) Cynomolgus monkeys received vehicle control and 10, 30, and

100 mg/kg of hBisAb on day 1 and 8 (n=1~3 monkey/group). The peripheral blood was collected at the indicated timepoint for hemoglobin (HGB) in response to the treatment. Ordinary one-way ANOVA with Dunnett's multiple comparisons test. (**B**) Principal-component analysis of RNA-seq samples from cyno peripheral blood receiving vehicle control or 100 mg/kg of hBisAb across all timepoints listed in Figure 7E. (**C**) *Cxcl10* gene expression change from baseline (0hr) comparing hBisAb- and vehicle-treated group across all timepoints (Student's unpaired T-test). (**D**) Volcan plot showing DEGs between hBisAb- and vehicle-treated group on 6h post-second dose on day 8. (**E**) IPA analysis of the DEGs from hBisAb-treated compared to vehicle group across all timepoints. (**F**) Gene correlation network analysis based on the interaction of top 100 up-regulated DEGs in hBisAb compared to vehicle group (fold change >2 and p-value > 0.05).

Supplementary Materials and Methods

Kinetic analysis

The analysis of affinities and kinetic binding constants of interactions between hBisAb and human, cynomolgus monkey, and mouse CD47 was performed by SPR using a Biacore T200 (Cytiva). hBisAb was immobilized on a surface via anti-human Fc antibody coupled to a CM4 chip and recombinant CD47 antigens were run over the surface as analytes. For PD-L1, the experiment was performed using neutravidin capture of biotinylated hBisAb and a single cycle kinetics methodology to capture the high-affinity interactions between hBisAb and PD-L1. The blocking activity of the interaction of SIRPα/CD47 and PD-1/PD-L1 was assessed in a biolayer interferometry binding assay (BLI), using an Octet HTX BLI instrument (Sartorius)

Production of αCD47/PD-L1 bispecific antibodies

For human and mouse bispecific antibodies, DNA sequences encoding αPD-L1 heavy chain, αCD47 heavy chain, and common lambda light chain were cloned into three separate mammalian expression vectors under the control of CMV-1 promoter using standard molecular biology techniques. For hBisAb, heterodimerization was achieved using 'knobs-into-holes' approach with αPD-L1 heavy chain harboring 'knob' mutations (T366W, Y349C) and αCD47 'hole' mutations (T366S, L368A, Y407V, S354C) in the human IgG1 background. For mBisAb, bispecific modality was achieved using 'R' mutations (T370K, K409R) in αPD-L1 heavy chain, and 'E' mutations (F405L, R411T) in αCD47 heavy chain in the mouse IgG2a background. In both cases 6xHis tag was added at the C-terminus of the αPD-L1 heavy chain to facilitate purification and separation of homodimeric monoclonal antibodies from desired heterodimeric bispecific antibody species. Expi293 cells were transfected transiently using 25 kDa PEIs (Polysciences) and all antibodies were expressed for 96 hours at 37°C.

Human bispecific antibodies were expressed after co-transfection of three chains (αPD-L1, αCD47 and common lambda light chain). Cells were harvested by centrifugation and resulting culture media was applied to ProteinA MabSelectSure column (Cytiva), purified according to manufacturer's protocol, and eluted proteins were dialyzed into PBS. Next, cation exchange column Source 15S (Cytiva) was used to separate homodimeric and heterodimeric species in 30 mM MES pH 6.0 buffer using gradients of 1 M NaCl (step 5-13% and linear 13-25%). Fractions containing hBisAb were dialyzed into PBS with 0.01% Tween-20 and frozen in aliquots at –80°C.

Mouse bispecific antibodies were purified from two separate monoclonal antibodies, followed by *in vitro* redox reaction to promote heterodimerization of the heavy chains. The αCD47 and αPD-L1 monoclonal antibodies were transfected as described above and culture media was purified using ProteinA MabSelectSure column (Cytiva) according to manufacturer's protocol, followed by desalting of eluted proteins into PBS using HiPrep 26/10 column (Cytiva). Equal amounts (mg:mg) of αCD47 and αPD-L1 monoclonal antibodies were mixed in PBS supplemented with 1 mM EDTA and 75 mM 2-MEA, and the reaction was incubated at 31°C with gentle shaking (300 rpm) for 5 hours. The reaction mixture was then buffer exchanged into PBS via dialysis to remove 2-MEA and EDTA and allow for mBisAb formation. Resulting reaction was then applied to cation exchange MonoS HR 16/10 GL column (Cytiva) and separated in 25 mM MES pH 5.5 buffer using 1 M NaCl linear gradient (1-100%). Fractions containing mBisAb were dialyzed into PBS and frozen in aliquots at –80°C.

Cell lines

CT26, B16F10, NCI-H292, HT1080 cells were obtained from the ATCC and cultured according to manufacturer's protocol. The MC38 murine colon carcinoma cell line was a gift from the Ribas Lab (UCLA) and were cultured in RPMI supplemented with 10% HI FBS, 1% Pen-Strep. CHO-

hPD-L1 and PD-1 Effector cells were obtained from Promega and cultured according to manufacturer's protocol. CHO-mPDL1 cells were obtained from GenScript and cultured according to manufacturer's protocol. CHO-hCD47 cells obtained from BPS Bioscience were cultured according to manufacturer's protocol. CHO-hCD47 cells and CHO-mCD47 cells were generated internally at Pfizer by stably transfecting CHO cells with human or mouse CD47 in pcDNA3.1(+) vector (Thermo Fisher Scientific) via G418 Sulfate selection media were cultured for the initial passages using CD CHO Medium supplemented with 10% HI FBS, 1% Pen-Strep plus 500 µg/ml of G418 Sulfate. All cell lines were cultured in a humidified chamber at 37°C under 5% CO2 atmosphere.

Animals

All mice studies were conducted according to the NIH animal care guidelines and following protocols approved by the Institutional Animal Care and Use Committee from Pfizer, Inc. C57BL/6, Balb/c, and Batf3-/- mice were obtained from the Jackson Laboratory and were 6-10 weeks of age at time of tumor inoculation. Human FcgR mice were bred in-house at Pfizer and were 30-38 weeks of age at time of tumor inoculation. Mice were of mixed sexes. Mice within experiments were age and sex matched. The NHP study was conducted in an AAALAC accredited facility (Pfizer, Groton, CT), in compliance with the Animal Welfare Act, the Guide for the Care and Use of Laboratory Animals, and the Office of Laboratory Animal Welfare. The procedures used in this study have been reviewed and approved by the Institutional Animal Care and Use Committee. Cynomolgus monkeys (> 2.5 yrs old, body weight range of 3.4-6.6 Kg) of Mauritius origin were sourced through Covance Primates, screened and randomly assigned to study treatment groups.

Purification of human monocytes from PBMCs and differentiation to macrophages

PBMCs were isolated from individual healthy donor buffy coats or leukopaks. Buffy coats from two healthy donors' whole blood were received from Stanford Blood Center. Twenty (25) mL of buffy coat was diluted with 75 mL PBS. Then 30 mL of diluted buffy coat was layered on top of 20 mL Ficoll-Paque PLUS (GE Healthcare) in SepMate50 PBMC Isolation Tubes and spun at 2,200 rpm for 20 minutes, at room temperature. The PBMC layer was transferred into a new 50 mL conical and washed with PBS. Samples were spun at 1,200 rpm for 5 minutes at room temperature. Following centrifugation, supernatant was removed, and cells were resuspended in 3 mL ACK Lysing Buffer and incubated at room temperature for 3 minutes. Thirty (30) mL of PBS was added to tubes and tubes were spun at 1,200 rpm for 5 minutes. Supernatant was removed and cells were resuspended in PBS containing 2% HI FBS for monocyte isolation. Leukopaks from healthy donors' whole blood were received from HemaCare. ACCUSPIN System-Histopaque1077 tube were brought to room temperature and centrifuged at 1,000 x g for 30 seconds at room temperature to assure that the liquid in the ACCUSPIN System-Histopaque1077 tube was below the frit, and then 15 to 30 mL of leukopak was poured into the upper chamber of each ACCUSPIN System-Histopaque1077 tube and spun at 1, 000 x g for 10 minutes at room temperature. After centrifugation, the plasma layer was aspirated within 0.5 cm of the opaque interface containing PBMCs. Then the PBMC layer was transferred into a new 50 mL conical tube and washed with PBS. Tubes were spun at 300 x g for 8 minutes. Following centrifugation, supernatant was removed, and cells were resuspended in 3 mL ACK Lysing Buffer and incubated at room temperature for 3 minutes. Thirty (30) mL of PBS was added to tubes and tubes were spun at 300 x g for 5 minutes. Supernatant was removed and cells were either resuspended in PBS containing 2% HI FBS for monocyte isolation or were cryopreserved in HI FBS with 10% DMSO

for future use. $CD14^+$ monocytes were enriched from PBMCs using a $CD14^+$ positive selection kit from Stem Cell Technologies according to manufacturer's protocol using the 'Big Easy' EasySep magnet. Enriched $CD14^+$ monocytes were cultured in cell culture media composed of RPMI 1640 supplemented with 10% HI FBS, 1% Pen-Strep at 1 x 10^6 monocytes/mL. The $CD14^+$ monocytes were differentiated into macrophages by the addition of 20 ng/mL of M-CSF for 6 to 7 days with additional media supplemented with 20 ng/mL M-CSF added 2 to 3 days post start of culture. On the day before the phagocytosis assay, media was aspirated and replaced with fresh cell culture media supplemented with 20 ng/mL of M-CSF and 10 ng/mL of IL-10 and cultured for overnight. Cells were grown in a humidified chamber at 37°C under 5% CO2 atmosphere.

Binding to human CD47 or human PD-L1 by flow cytometry

CHO-hCD47 or CHO-hPD-L1 cells were assayed to determine the cell-based binding human CD47 EC50 or human PD-L1 EC50 for test compounds by flow cytometry. Cells were collected using TrypLE Express Enzyme, pelleted, and resuspended with FACS Buffer (PBS + 2% HI FBS). 50,000 cells were plated per well in 96-well round bottom plate and incubated with titrating doses of test compounds for 30 minutes on ice. Cells were washed with FACS buffer and resuspended with 100 µL of a 1:100 dilution of APC-labeled anti-hIgG (Fcγ Fragment Specific) antibody per well and incubated in the dark on ice for 30 minutes. Cells were washed and resuspended in cold FACS Buffer for data acquisition using a BD Fortessa. Data analysis was performed using Flowjo software. EC50 was then determined by non-linear regression plot of *log(agonist) vs. response – variable slope (four parameters)* with bottom and top constraints set in GraphPad Prism software.

SIRPα-CD47 blocking assay

CHO-hCD47 cells from BPS Bioscience and CHO-mCD47 generated in house were assayed to determine the cell-based SIRPα blocking IC50 for test compounds by flow cytometry. Cells were

collected using TrypLE Express Enzyme, pelleted, and resuspended in FACS Buffer (PBS + 2% HI FBS). 50,000 cells were plated per well in 96-well round bottom plate and incubated 1ug/well of recombinant SIRP alpha/CD172a Fc chimera protein and titrating doses of test compounds for 30 minutes on ice. After incubation, cells were washed with FACS buffer and resuspended with 100 µL of a 1:100 dilution of APC anti-human SIRPα/β antibody or APC-anti-mouse SIRPα per well and incubated in the dark on ice for 30 minutes. Cells were washed twice with FACS buffer and resuspended in cold FACS Buffer for data acquisition using a BD Fortessa. The cell-based hSIRPα blocking graph shows the percentage of SIRPα bound on CHO-hCD47. The cell-based mSIRPα blocking graph shows the APC MFI on CHO-mCD47. The cell-based SIRPα blocking IC50 value was determined by non-linear regression plot of log(inhibitor) vs. response – variable slope (four parameters) in GraphPad Prism software using the APC MFI (Median Fluorescence Intensity). Data analysis was performed using Flowjo software.

Human PD-1-PD-L1 TCR NFAT bioassay

The PD-1/PD-L1 blockade TCR NFAT bioassay (Promega) was used for the *in vitro* blocking activity of test compounds on the PD-L1/PD-1 axis. Adherent CHO-PD-L1 cells were collected using TrypLE™ Select Enzyme. Cells were centrifuged at 230 × g for 10 minutes and resuspended in cell recovery medium (Ham's F-12 Nutrient Mix supplemented with 10% HI FBS) to a concentration of 3×10^5 viable cells/ml. 30,000 cells were plated per well in a white, flat-bottom 96-well assay plate and incubated overnight in at 37°C under 5% CO2 atmosphere. The next day PD-1 effector cells were prepared by pelleting the cells at 130–180 × g for 10 minutes at ambient temperature and resuspending in assay buffer (RPMI 1640 with L-glutamine supplement with 1% HI FBS) to a concentration of $1.25x10^6$ cells/mL. Cell recovery medium was removed from the white, flat-bottom 96-well assay plate containing pre-plated CHO PD-L1 cells. $5x10^4$ PD-1

Effector cells were plated per well and incubated with titrating doses of test compounds for 6-24hrs at 37°C under 5% CO2 atmosphere. After incubation, assay plates were removed from the incubator and equilibrated to ambient temp for 5-10 minutes. Bio-Glo Reagent was added to the inner 60 wells of the assay plates and incubated at ambient temperature for 5–30 minutes. Then luminescence was measured using a luminescence plate reader. Data analysis was performed using Excel and Prism. Fold induction was calculated using the following formula Calculate fold induction = RLU (induced)/RLU (no antibody control). The TCR EC50 was determined by non-linear regression plot of log(agonist) vs. response – variable slope (four parameters) with bottom and top constraints set in GraphPad Prism software.

Mouse PD-1/PD-L1 blocking assay

CHO-mPD-L1 cells from GenScript were assayed to determine the cell-based mPD-L blocking IC50 for test compounds by flow cytometry. Cells were collected using TrypLE Express Enzyme, pelleted, and resuspended in FACS Buffer (PBS + 2% HI FBS). 50,000 cells were plated per well in 96-well round bottom plate and incubated 0.6 ug/well of Recombinant Mouse PD-1 Fc Chimera Protein and titrating doses of test compounds for 30 minutes on ice. After incubation, cells were washed with FACS buffer and resuspended with 100 µL of a 1:200 dilution of APC-labeled anti-hIgG (Fcγ Fragment Specific) per well and incubated in the dark on ice for 30 minutes. Cells were washed twice with FACS buffer and resuspended in cold FACS Buffer for data acquisition using a BD Fortessa. The cell-based mPD-1 blocking graph shows the APC MFI on CHO-mPD-L1 cells as determined by non-linear regression plot of log(inhibitor) vs. response – variable slope (four parameters) in GraphPad Prism software using the APC MFI (Median Fluorescence Intensity). Data analysis was performed using Flowjo software.

***In vitro* binding selectivity assay**

To determine RBC versus tumor cell binding selectivity of test compounds, RBCs and CFSE labeled tumor cells were co-cultured at a 1:1 ratio with test compounds. Adherent HT1080 or MC38 cells were collected using TrypLE Express Enzyme and pelleted. Tumor cells were stained with 4ul CFSE stock solution for 10 minutes at 37°C under 5% CO2 atmosphere. CFSE labeled tumor cells were washed, pelleted, and resuspended at 2.5 x 10^6 cells/mL in FACS buffer. Human or murine RBCs were counted using a hemacytometer and cell density was calculated. The required number of RBCs were aliquoted and resuspended at 2.5 x 10^6 cells/mL in FACS buffer. Test compounds were diluted in FACS buffer (PBS containing 2% HI FBS) serial dilutions were prepared. Fifty thousand (50,000) CFSE labeled tumor cells and 50,000 RBCs were plated per well in 96-well round bottom plates and incubated with test compounds for 30 minutes on ice. Cells were washed with PBS and resuspended with 100 µL of a 1:200 dilution of AF647-labeled anti-hIgG (Fcγ Fragment Specific) or APC-labeled anti-mIgG (Fcγ Fragment Specific) antibody per well and incubated in the dark on ice for 30 minutes. Cells were washed with FACS buffer and analyzed on a Fortessa with FACS Diva software (BD Biosciences). CFSE was detected as FITC and AF647 was detected as APC on the Fortessa. Tumor cells were defined as FITC+ and RBCs were defined as FITC negative (FITC). Cells that stained positive for APC (APC+) were defined as antibody bound cells. The frequency of APC+ cells within the FITC+ population or FITC- population was used as the 'percentage of antibody-bound cells per cell type'. The frequencies were exported from Flowjo and analyzed in PRISM. The tumor and RBC binding EC_{50} values were determined by non-linear regression plot of log(agonist) vs. response – variable slope (four parameters*)* with bottom and top constraints set in GraphPad Prism software. Treatment concentrations plotted as agonist. Percentage of antibody-bound cells per cell type was plotted as

response. Bottom constraint equal to the 0% antibody bound. Top constraint equal to the 100% antibody bound.

Phagocytosis assay

To test antibody-induced phagocytosis of IFNg treated NCI-H292 cells by monocyte-derived macrophages, NCI-H292 cells were treated with 10 ng/mL of recombinant human IFNg overnight to increase PD-L1 expression. NCI-H292 cells were used as a representative tumor cell line. On the day of the assay, adherent NCI-H292 cells and macrophages were treated with TrypLE. The cells were collected in 50 mL conical tubes and pelleted by centrifugation at 1,200 rpm for 5 min, and then supernatant aspirated and resuspended in 1 mL of PBS for CSFE and CTV staining. Stock solutions of CFSE and CTV were prepared by dissolving the contents of one vial of CFSE or CTV (lyophilized powder) with 50 µL of DMSO prior to use. To stain NCI-H292 cells, 2 µL of CFSE stock solution was added to 1 mL of cells. To stain macrophages, 2 to 4 µL of CTV stock solution was added to 1 mL of cells. The cells were incubated for 10 minutes at 37°C under 5% CO2 atmosphere. After 10 minutes of staining cells, 15 mL of PBS was added to tube and cells were centrifuged at 1,200 rpm for 5 minutes. CFSE stained NCI-H292 cells were resuspended to in assay media (RPMI 1640 supplemented with 10% HI FBS and 1 % Penstrep). CTV stained macrophages were resuspended in assay media. Test compounds were diluted in assay media and 7-point 5-fold serial dilutions were prepared. Twenty-five thousand (25,000) CFSE labeled, IFNg treated NCI-H292 cells and 50,000 CTV labeled macrophages were plated per well in 96-well round bottom plates and incubated with test compounds (dose range 0.0128 nM to 200 nM) for 2 hours at 37°C under 5% CO2 atmosphere. After incubation, co-cultures were washed with 100 µL PBS and spun down at 1,200 rpm for 5 minutes. Supernatant was removed and each well resuspended in 120 µL of FACS Buffer (PBS supplemented with 2 % HI FBS). Then each well

was acquired on the Fortessa with FACS Diva software. CFSE was detected as FITC and CTV was detected as BV421 on the Fortessa. For each well, 5,000 FITC+ events were collected. Data analysis was performed using FlowJo software. Samples were gated to exclude doublets. Tumor cells were defined as FITC+ and macrophages were defined as BV421+. Cells that were FITC+BV421+ were defined as tumor cells phagocytosed by macrophages. Cells that were FITC+BV421- were defined as non-phagocytosed tumor cells. The number of events for phagocytosed and non-phagocytosed tumor cells were exported from FlowJo into Excel. In Excel, the percent phagocytosis of total tumor cells was calculated using the following formula:

(No. of phagocytosed tumor cells) / (No. of phagocytosed tumor cells + No. of non-phagocytosed tumor cells) * 100 = Phagocytosis % of Total Tumor

Percent phagocytosis of total tumor cells was plotted in GraphPad Prism Software.

MLR assay

LPS matured DCs were prepared. Isolated human PBMC were resuspended to $1x10^6$ cell/ml with Serum-Free RPMI Medium 1640 (Gibco A10491-01) and incubated at 37 degree incubator for 3 hrs. Then supernatant was discarded, RPMI 1640 Medium + 10 %FBS (Biological Industries 04-002-1A) with 250U/ml IL-4 (Peprotech 200-04) and 500 U/ml GM-CSF (Peprotech 300-03) was added and cell were incubated in 37 degree incubator for 5-7 days. Then the DCs were matured with 1μg/ml LPS (sigma L6529) in RPMI 1640 Medium + 10 %FBS for about 24 hrs. CD4+ T cells were isolated from a freshly isolated human PBMC (different donor than DCs) according to the kit (Easysep human CD4+ T cell isolation, Stemcell#17952). 200,000 purified CD4+ T cells and 50,000 matured DC were added to 96 well plate with test compounds. Samples were incubated at 37 degree for 72 hours for IL-2 detection and 120 hours for IFN-gamma detection. Supernatants were harvested at 72 and 120 hours and frozen at -20 degree for ELISA assay. IL2 was detected

in supernatant by ELISA kit (R&D#DY202) according to manufacturer protocol. IFNg was detected in supernatant by ELISA kit (R&D#DY285B) according to manufacturer protocol.

Preparation of single cell suspension from mouse tissues

For characterization of splenic and tumor infiltrating T cell populations, spleens were mechanically dissociated by processing over a 40uM nylon mesh filter before treatment with HybriMAX Red Blood Cell Lysing Buffer (Sigma Aldrich) at room temperature for 5 minutes, and tumors were dissociated and processed to a single suspension using the Mouse Tumor Dissociation Kit (Miltenyi Biotec) according to manufacturer's instructions.

For assessment of *in vivo* binding selectivity, tumors were mechanically dissociated by using the gentleMACS OCTO Dissociator and then filtered over 70uM nylon mesh filter. Blood samples were collected in heparin diluted 1:20 in PBS, then samples were washed with FACS buffer (PBS + 2% Heat Inactivated FBS)

For characterization of splenic and tumor infiltrating T cell populations by CyTOF, spleens were treated for 25 minutes at 37 degrees with 25 ug Liberase TL (Roche) then mechanically dissociated by processing over a 70uM nylon mesh filter before treatment with ACK Lysis Buffer (Gibco) at room temperature for 3 minutes. Tumor samples were dissociated and processed to a single suspension using the Mouse Tumor Dissociation Kit (Miltenyi Biotec) according to manufacturer's instructions except for 10% less than recommended amount of the R enzyme was used per sample. Single cell suspension of tumor samples were then enriched for CD45+ cells using the Miltenyi mouse CD45(TIL) Microbeads Kit (Miltenyi BioTec) according to manufacturer's instructions for the LS columns.

For characterization of splenic and tumor infiltrating T cell populations by scRNA-seq, spleens were processed to a single cell suspension using the same method used for processing spleens in the CyTOF study. Tumors were mechanically dissociated according to the protocol used for *in vivo* binding selectivity. Single cell suspension of tumor samples were then enriched for CD45+ cells using the Miltenyi CD45 MicroBeads Kit (Miltenyi BioTec) according to manufacturer's instructions.

Mass Cytometry (CyTOF)

Mass-tagged Antibodies

A list of all mass cytometry antibodies and their labelled isotopes are summarized in Supplementary Table 9. Pre-conjugated metal-tagged antibodies were purchased from Fluidigm when available. For all other antibodies, purified formulations were purchased from the companies indicated in Supplementary Table 9, and conjugated using the Maxpar® X8 Antibody Labelling Kit (Fluidigm) according to the manufacturer's protocol.

Mass Cytometry Surface and Intra-cellular Straining

Three million CD45+ TIL enriched cells from each sample were washed with PBS (minus Ca^{2+} and Mg^{2+}) (Gibco) to remove soluble proteins, and labelled with Cell-ID™ Cisplatin-198Pt (Fluidigm) for 5 minutes to measure viability. Cells were then washed with Maxpar® Cell Staining Buffer (SB) (Fluidigm) and normalized to 100 µL of residual volume before surface marker staining for 40 mins. at room temperature. Cells were blocked with 5 µL of purified anti-mouse CD16/32 (clone 93) antibody (Biolegend) for 5 mins. prior to staining. Cells were then washed with SB before they were fixed and permeabilized using the eBioscience™ Foxp3/Transcription Factor Staining Buffer Set (Invitrogen™, Waltham, USA). Cells were normalized to 100 µL

residual permeabilization buffer, before intra-cellular marker staining for 40 mins. at room temperature. Cells were washed once more with permeabilization buffer, and then washed with SB before mass-tagged barcoding. After barcoding and pooling all samples into batches, each batch was diluted to $2x10^6$ cells/mL of DNA-Ir solution and stored at 4°C for up to 10 days prior to acquisition on the Helios™ (Fluidigm) mass cytometer. DNA-Ir consists of 2.0% (w:v) EM Grade Paraformaldehyde (Catalog#15710, Electron Microscopy Sciences) in PBS, with 125 nM Cell-ID™ Intercalator-Ir (Fluidigm).

Mass-tagged Cellular Barcoding

All samples were labelled per manufacturer's protocol, with metal-tagged cellular barcodes using the Cell-ID™ 20-Plex Pd Barcoding Kit (Fluidigm). Barcoded samples were pooled into batches of up to 20 samples, so that no two samples shared the same hexameric barcode within each batch. Each individual sample within each batch was reidentified by manual boolean gating of palladium (Pd) isotopes ^{102}Pd, ^{104}Pd, ^{105}Pd, ^{106}Pd, ^{108}Pd, and ^{110}Pd, and then exported as its own FCS file.

Acquisition & Bead Standard Data Normalization

An aliquot from each batch, was washed twice with SB and then twice with ≥18.2 MΩ.cm Milli-Q® ultrapure water (MilliporeSigma). Aliquots were stored as a pellet in residual volume for no longer than 16 hours at 4°C. Right before acquiring, each aliquot was filtered through a 35 μm nylon mesh (Catalog# 352235, Falcon), and resuspended to $1.0x10^6$ cells/mL of diluted (1:4 parts) EQ™ Four Element Calibration Beads (Fluidigm). Instrument tuning was performed once per day of operation according to manufacturer's protocol, unless a part was replaced in which cased tuning was run again. An event rate of 500 per second or less was maintained for all aliquots. Using the PSI injection system, a sample line pressure of <20 PSI was maintained by intermittent cleaning using 2.0% (v:v) nitric acid and manual backflushing, or by replacing parts that had

impeded flow due to sample clogging. All recorded FCS data was randomized, using the uniform negative distribution method, and was bead-normalized, using median bead intensity at 100 second intervals, with the instrument's CyTOF® Software (v6.0).

Individual sample FCS data were manually gated using OMIQ SaaS (Omiq Inc.) to exclude normalization beads, cell debris, dead cells, technical artifacts, and doublets for the identification of live CD45+ cells prior to downstream analyses.

Flow cytometry

For characterization of splenic and tumor infiltrating T cell populations, single cell suspensions from tumor and spleen were stained with the following surface antibodies in a 1:1 dilution of Staining Buffer (Biolegend) and BD Horizon Brilliant Stain Buffer (BD Biosciences) for 10 minutes on ice: anti-CD45, NK1.1, CD19, CD4, CD8a, CD3, TCRb, CD25, CD44, CD62L, and Lag3. Samples were then stained in LIVE/DEAD Fixable Blue Cell Stain Kit (Thermo Fisher Scientific) at 1:1000 in PBS on ice for 10 minutes. Following fixation for 30 minutes on ice using the FoxP3 Transcription Factor Staining Buffer Set (Thermo Fisher Scientific), cells were incubated with intracellular antibodies (anti-Ki67 and Tcf1) in permeabilization buffer for 8 hours at 4C. Samples were washed twice prior to acquisition on an Aurora (Cytek). Additional details regarding the specific antibodies used for flow cytometric analysis are provided in Supplementary Table 9.

For assessment of *in vivo* binding selectivity, blood samples and single cell suspension from tumor and spleen were stained in mouse Fc block (BD) at 1:25 and LIVE/DEAD Fixable Blue Cell Stain Kit (Thermo Fisher Scientific) at 1:100 in FACS buffer at room temperature for 10 minutes. Then samples were stained with the following surface antibodies in a 1:1 dilution of FACS buffer and BD Horizon Brilliant Stain Buffer (BD Biosciences) for 1 hour on ice: anti-CD45, anti-B220, anti-

Thy1.2, anti-CD4, anti-CD8, anti-NKp46, anti-CD11b, anti-CD11c, anti-F4/80, anti-Ly6C, anti-Ly6G, anti-IL4R and anti-human IgG (Jackson ImmunoResearch). Samples were washed twice prior to acquisition on an Fortessa (BD).

Single-cell RNA-seq and data processing

Tumors were harvested and viable CD45+ cells were FACS sorted from control, αmCD47, αmPD-L1, αmCD47 and αmPD-L1 combination, and mBisAb-treated mice (n = 4~5/group). Single-cell emulsions were obtained using the 10X Genomics Controller and the v2 library and Gel Bead kit (10x Genomics). RNA-sequencing libraries were prepared as instructed by the 10x 3' v2 kit protocol. Resulting libraries were sequenced on an Illumina NextSeq using a NextSeq 500/550 v2.5 High Output Kit. Cell Ranger 3.0.2 (https://support.10xgenomics.com/) was used to process single-cell sequencing data and generate the matrix data containing gene counts for each cell per sample. Briefly, raw base call files from Illumina sequencers were first demultiplexed into FASTQ files with the "cellranger mkfastq" pipeline. Then, the "cellranger count" was used to align FASTQs files to the mouse reference genome (mm10) followed by reads filtering, barcode counting, and UMI counting. Finally, the gene expression matrixes of all samples were imported into Seurat v3(3.2.3). The following filtering steps were carried out to exclude low-quality cells: (a) cells with fewer than 200 detected genes and/or (b) cells with greater than 10% mitochondrial reads were discarded. As a result, a total of 13667 cells (2269 from control, 2319 from αmCD47-treated, 2915 from αmPD-L1-treated, 2239 from αmCD47 and αmPD-L1 combination-treated, 3925 from mBisAb-treated) with 17556 informative genes were included in the downstream analyses.

Clustering of single cells, trajectory analysis, and definition of cell states

The gene expression data were log-normalized and scaled with default parameters. The top 2,000 most variable genes identified by Seurat function "FindVariableFeatures" were used for the principal component analysis (PCA). The first 40 principal components (PCs) selected based on the ElbowPlot were used for clustering analyses. Cell clusters were identified using FindClusters functions implemented in Seurat with default parameters and resolution parameter as 0.9. The t-SNE and UMAP were used to visualize the clustering results with default parameters. Myeloid cells and lymphocytes were further separated into different subtypes based on the same procedures. Machine learning algorithm Random Forest and our in-house reference databases were used to annotate the cell type of large cell populations. The cell types of clusters and subclusters were further confirmed and annotated by comparing the specifically expressed genes identified by the Seurat "FindAllMarkers" function with the known cell markers reported in the literature. Pathway scores were calculated by Suerat function "AddModuleScore" which calculate the average signature gene expression of each cluster subtracted by the aggregated expression of control gene set.

The myeloid cell subpopulations of interest were selected for single-cell trajectory analysis. Using Monocle (v2.0), cells were ordered according to their inferred pseudotime by following the steps described on Monocle documentation (http://cole-trapnell-lab.github.io/monocle-release/docs/). Only the top 100 differentially expressed genes among myeloid clusters were used for dimensionality reduction and trajectory reconstruction. The reduce Dimension function with DDRTree as the reduction method was applied to the top principal components (PCs) and projected the cells onto two dimensions. After the dimension was reduced, the "orderCells" function was used to order cells and the plot_cell_trajectory function was used to visualize the trajectory in two-dimensional spaces.

Gene expression analysis in mice

Total RNA (50–100 ng) was used in the nCounter assay (NanoString Technologies) using mouse-specific nCounter PanCancer Immune Profiling and PanCancer Pathways Panels supplemented with custom-made 30-plex code set or human-specific nCounter PanCancer Immune Profiling Panel following the manufacturer's recommendations. Samples were prepared using an nCounter Prep Station, and code set/RNA complexes were immobilized on nCounter cartridges for data collection; data were collected on a NanoString Digital Analyzer. nCounter RNA count data were normalized using the geometric mean of the positive controls and HKGs. Extensive quality control analysis was applied to raw and normalized data to identify batch effects and issues with control probes and the samples. A LLOD threshold was set for the counts on the basis of the maximum count of the background controls (negative). Genes with normalized counts less than LLOD were flagged as low-expressing genes. The curated data were subjected to statistical analysis using ANOVA tests followed by pathway analysis using IPA and GSEA.

Gene expression analysis in NHP

RNAseq sequences were aligned to Cyno genome (Macaca_ fascicularis_5.0.93 assembly and gtf) and gene expression quantification was performed by RSEM software (v1.3.0) using default parameters to calculate log2 TPM values. Differential gene expression analysis was performed using Limma (v3.38.3) with differentially expressed (DE) genes defined as those with adjusted p value <0.05 and fold-change > 1. Pathway analysis was performed on DE genes using "enricher" function in "clusterProfiler" R package (v3.14.3) and IPA database. Log2 transformed gene expression estimates (tag count per million, TPM) were used for the heatmaps. Relative expression to the baseline (0 hr) was plotted in the boxplot when comparing across different treatments and timepoints. LM22 (22 immune cell types) scores from all samples were calculated using average

expression of the genes in each signature. LM22 is a specific gene signature containing 547 genes that distinguish 22 immune cell subtypes downloaded from the CIBERSORT web portal (http://cibersort.stanford.edu/).